Surface Plasmon-Polariton Enhanced Lasing: Numerical Studies

by

Andre J. Brewer

A Thesis Presented in Partial Fulfillment
of the Requirements for the Degree
Master of Science

Approved April 2017 by the
Graduate Supervisory Committee:

Maxim Sukharev, Co-Chair
Daniel E. Rivera, Co-Chair
José Menéndez

ARIZONA STATE UNIVERSITY

May 2017

ABSTRACT

The study of subwavelength behavior of light and nanoscale lasing has broad potential applications in various forms of computation i.e. optical and quantum, as well as in energy engineering. Although this field has been under active research, there has been little work done on describing the behaviors of threshold and saturation. Particularly, how the gain-molecule behavior affects the lasing behavior has yet to be investigated.

In this work, the interaction of surface-plasmon-polaritons (SPPs) and molecules is observed in lasing. Various phenomenologies are observed related to the appearance of the threshold and saturation regions. The lasing profile, as a visual delimiter of lasing threshold and saturation, is introduced and used to study various parametrical dependencies of lasing, including the number-density of molecules, the molecular thickness and the frequency detuning between the molecular transition frequency and the SPP resonant frequency. The molecular population distributions are studied in terminal and dynamical methods and are found to contain unexpected and theoretically challenging properties. Using an average dynamical analysis, the simulated spontaneous emission cascade can be clearly seen.

Finally, theoretical derivations of simple 1D strands of dipoles are presented in both the exact and mean-field approximation, within the density matrix formalism. Some preliminary findings are presented, detailing the observed behaviors of some simple systems.

ACKNOWLEDGMENTS

TABLE OF CONTENTS

CHPATER

CHAPTER

LIST OF FIGURES

I. INTRODUCTION

A. Opening

The following is a comprehensive presentation of detailed computational and theoretical work on the subject of lasing systems – particularly on the gain media of 4-level molecules in 2-dimensions. The author had completed a simpler work of this nature previously in 1-dimension, this being the natural extension. The personal motivation to pursue the in-depth research presented, apart from the academic, is not only to advance the general research enterprise, but to grow as a physicist, in the hope of benefiting humanity with current and subsequent findings.

The work is meant to be taken as a comprehensive whole, however, the reader is encouraged to customize the experience as deemed necessary as many sections can stand alone.

1) Motivation

Control and behavior of light under ordinary circumstances is limited to the diffraction limit and wavelength of the radiation of interest. For visible light, that range is approximately 400 nm to 700nm. This is not the complete story, however. A variety of plasmons can be supported by various materials [1] which will be described in more detail in Section I-C3, but are collective excitations of the electrons in a metal [2]. These plasmons are due to evanescent fields caused by internal reflection. The primary interest in them is that the radiation is localized by at least an order of magnitude smaller than the vacuum wavelength [1]. With this subwavelength control, a variety of possibilities and

application have been proposed such as advances in lenses and optical nonlinearities [3] to optical and quantum computers [4].

To understand and thereby advance these proposed applications, research has been growing to develop accurate and useful, self-consistent models that describe the plasmons and their coupling to various materials [5], [6], [3], and [7]. Since metals cause high optical loss, much concentration has been put into coupling plasmons with lasing material to compensate [8]. This work develops a model, similar to the state-of-the-art and demonstrates various features and behaviors. Of particular emphasis in this work is, however, the behavior of the gain medium interacting with the plasmons. This is an area that seems to have been left behind. The semi-classical model for the gain medium developed in Section I-C4 is rather standard. Since the model produces experimentally verifiable results, it has remained largely unexplored, and the behavior of the gain material is rarely, if ever, discussed. This work endeavors to investigate the various features of lasing with Plasmon-molecule coupled lasing systems, particularly asking the questions: *why* does lasing occur? *what* happens in the gain medium? And *how* does the gain material behave? As these questions are quite ambitions and usually lead to more questions, this work presents findings up-to-date and will hopefully lead to the answering of the above questions, and perhaps development of better theory and understanding.

2) Opening Summary

Now, to provide the reader with a brief orientation on the layout of this work. This first section provides relevant theory and background to appreciate the work. Section II details computational research completed on lasing system, with computational analysis into the

2

molecular dynamics. Section III lays the groundwork for a deeper theoretical endeavor to compare the exact quantum formulation of the gain medium, and the mean-field approximation used in Section II and almost every other work of this nature. A few parting words and summary are given in Section IV.

B. Simulated System

Before a discussion of the physics given, a description of the system under simulation will motivate the physics needed and provide a mental picture of what the work is all about. The system is a periodic structure of silver nanoslits with a nanolayer of 4-level molecules as the gain medium, depicted below.
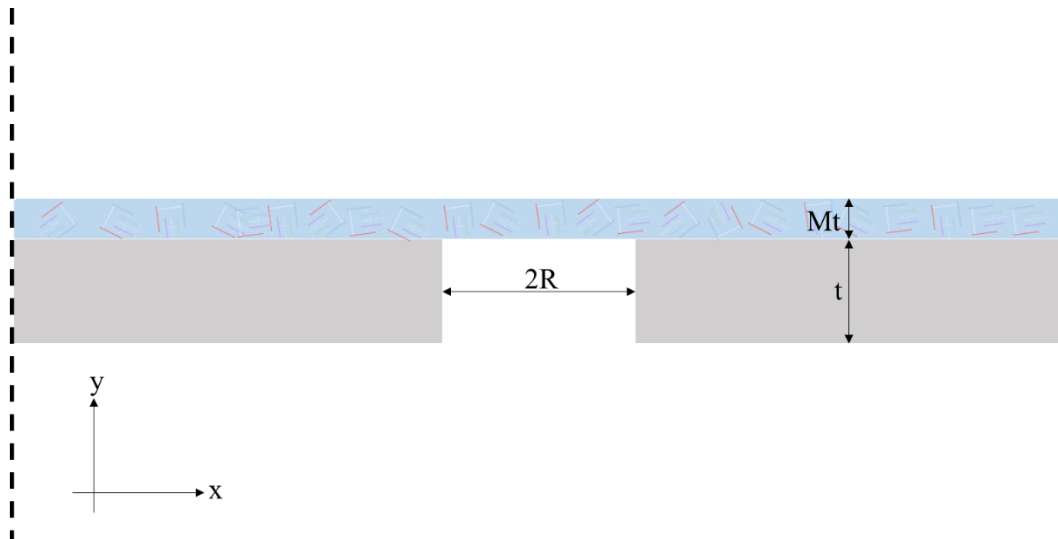
Figure 1: Rendition of the Simulated System. The Gray is the silver (Ag), the blue is the molecular layer. The dotted lines depict the periodicity. The nanoslit geometrical parameters are R and t. One of the molecular layer parameters is the thickness, Mt.

The parameters governing the geometry of the silver nanoslits are the slit radius, R, and the thickness, t, keeping in mind that the z-axis extends to infinity. The periodicity is

depicted by the dotted lines. The molecular layer, has the geometric parameter of its thickness, Mt. The little levels depicted in the molecular layer will become apparent in Section I-C4.

C. The Physics

All proper academic endeavors are set apart from the ordinary, the simplistic and the metaphysical by, in addition to concrete analysis and testing, having a firm foundation in previous work and a concrete (or the closest possible) understanding of empirically confirmed theory. This work endeavors no less. The following will deliver to the reader the most cogent aspects of relevant theory to understand and appreciate the work. Following, the computational aspects of this work will be presented including the famous *Yee's Algorithm* and the implementation of the simulation system.

1) Maxwell's Equations and Modes

Perhaps one of the most seminal works in physics was the development of a comprehensive and self-consistent description of electric and magnetic phenomena. Maxwell is regarded as the progenitor of the famous *Maxwell's Equations*. While Maxwell did connect the known phenomena together in his work and was the first to successfully predict the speed of light theoretically, he developed 20 equations and were somewhat difficult use. Oliver Heaviside was the one that packaged Maxwell's discoveries into the form in which we are familiar today [9]:

$$\nabla \cdot \vec{E} = \frac{1}{\epsilon_0}\rho \tag{1.1}$$

$$\nabla \times \vec{E} = -\frac{\partial \vec{B}}{\partial t} \tag{1.2}$$

$$\nabla \cdot \vec{B} = 0 \tag{1.3}$$

$$\nabla \times \vec{B} = \mu_0 \vec{J} + \mu_0 \epsilon_0 \frac{\partial \vec{E}}{\partial t} \tag{1.4}$$

For propagation in matter, the auxiliary fields are used and since the gradient equations can be derived from the curl equations, the equations necessary for simulation are given as the following with the appropriate adjustments made for propagation in matter:

$$\nabla \times \vec{E} = -\mu \frac{\partial \vec{H}}{\partial t} \tag{1.5}$$

$$\nabla \times \vec{H} = \sigma \vec{E} + \epsilon \frac{\partial \vec{E}}{\partial t} \tag{1.6}$$

The simulations in this work are 2-D, or there is one dimension (z for this work) in which there are no changes a.k.a. the derivatives with respect to the third dimension are all zero. In practical applications, this means that one dimension is *comparably* infinite to the other two dimensions i.e. the vertical dimension of a system is in μm and the horizontal dimensions are in nm. Carrying out simulations in 2-D greatly reduces computational complexity while still being useful in physical investigations. An interesting physical phenomenon can be shown if the curl equations are written in component form:

$$\begin{aligned}
\frac{\partial E_z}{\partial y} - \frac{\partial E_y}{\partial z} &= -\mu \frac{\partial H_x}{\partial t} \\
\frac{\partial E_x}{\partial z} - \frac{\partial E_z}{\partial x} &= -\mu \frac{\partial H_y}{\partial t} \\
\frac{\partial E_y}{\partial x} - \frac{\partial E_x}{\partial y} &= -\mu \frac{\partial H_z}{\partial t} \\
\frac{\partial H_z}{\partial y} - \frac{\partial H_y}{\partial z} &= \sigma E_x + \epsilon \frac{\partial E_x}{\partial t} \\
\frac{\partial H_x}{\partial z} - \frac{\partial H_z}{\partial x} &= \sigma E_y + \epsilon \frac{\partial E_y}{\partial t} \\
\frac{\partial H_y}{\partial x} - \frac{\partial H_x}{\partial y} &= \sigma E_z + \epsilon \frac{\partial E_z}{\partial t}
\end{aligned} \tag{1.7}$$

In 2-D, as mentioned, the spatial derivatives of the *comparably* infinite dimension are null, therefore eliminating the spatial derivatives of z:

$$\text{TM Mode} \begin{cases} \dfrac{\partial E_z}{\partial y} = -\mu \dfrac{\partial H_x}{\partial t} \\[2mm] \dfrac{\partial E_z}{\partial x} = \mu \dfrac{\partial H_y}{\partial t} \\[2mm] \dfrac{\partial H_y}{\partial x} - \dfrac{\partial H_x}{\partial y} = \sigma E_z + \epsilon \dfrac{\partial E_z}{\partial t} \end{cases}$$
$$\text{TE Mode} \begin{cases} \dfrac{\partial E_y}{\partial x} - \dfrac{\partial E_x}{\partial y} = -\mu \dfrac{\partial H_z}{\partial t} \\[2mm] \dfrac{\partial H_z}{\partial y} = \sigma E_x + \epsilon \dfrac{\partial E_x}{\partial t} \\[2mm] \dfrac{\partial H_z}{\partial x} = -\sigma E_y - \epsilon \dfrac{\partial E_y}{\partial t} \end{cases} \tag{1.8}$$

The component forms have been grouped into two modes given the names *Transverse Magnetic* and *Transverse Electric* modes. Notice that each of the modes requires no information from the other mode. Since these two modes are independent, only one need be simulated, again, reducing computational complexity. As was described in Section I-B, the system under simulation is infinite in the *z-dimension*. Only the TE mode will stimulate plasmon phenomena and is the only mode simulated. To demonstrate that the TE mode contains the necessary information to fully describe the EM wave phenomena, the following derivatives are taken:

$$\frac{\partial}{\partial t}\left[\frac{\partial E_y}{\partial x} - \frac{\partial E_x}{\partial y} = -\mu_0 \frac{\partial H_z}{\partial t}\right] \rightarrow \frac{\partial^2 E_y}{\partial t \partial x} - \frac{\partial^2 E_x}{\partial t \partial y} = -\mu_0 \frac{\partial^2 H_z}{\partial t^2}$$
$$\frac{\partial}{\partial y}\left[\frac{\partial H_z}{\partial y} = \sigma E_x + \epsilon \frac{\partial E_x}{\partial t}\right] \rightarrow \frac{\partial^2 H_z}{\partial y^2} = \sigma \frac{\partial E_x}{\partial y} + \epsilon \frac{\partial^2 E_x}{\partial t \partial y} \tag{1.9}$$
$$\frac{\partial}{\partial x}\left[\frac{\partial H_z}{\partial x} = -\sigma E_y - \epsilon \frac{\partial E_y}{\partial t}\right] \rightarrow \frac{\partial^2 H_z}{\partial x^2} = -\sigma \frac{\partial E_y}{\partial x} - \epsilon \frac{\partial^2 E_y}{\partial t \partial x}$$

And upon addition of the three resulting equations:

$$\frac{\sigma}{\epsilon} \frac{\partial E_y}{\partial x} - \frac{\sigma}{\epsilon} \frac{\partial E_x}{\partial y} + \frac{1}{\epsilon} \frac{\partial^2 H_z}{\partial x^2} + \frac{1}{\epsilon} \frac{\partial^2 H_z}{\partial y^2} = \mu_0 \frac{\partial^2 H_z}{\partial t^2} \tag{1.10}$$

The underlined portion is one of the 2-D wave equations. The extra curl portion is only relevant in matter. In vacuum, $\sigma = 0$ and the standard wave equation is recovered. The TE mode equations form the backbone of the simulations. In vacuum, they are complete. In the metal and the molecular layer however, more theory is needed.

2) Drude Model

For the electric fields in the silver, the Drude model is used. Around 1900, Drude developed the first iteration of what is known as the Drude model by assuming the electrons in a metal formed an ideal gas, using the classical equation of motion [2]:

$$m\dot{v} + \frac{m}{\tau} v_D = -eE \tag{1.11}$$

where m is the electron mass, τ is a relaxation time, v_D is a frictional term, e is the elementary charge unit, and E is the external field. Derivations are plentiful and will not be shown here. The final expression for the relative permittivity is given by [10]:

$$\epsilon(\omega) = \epsilon_\infty - \frac{\omega_p^2}{\omega^2 - j\omega\gamma_p} \tag{1.12}$$

where ω_p is the pole frequency and γ_p is the inverse relaxation time.

3) Plasmons

Plasmons refer to the collective excitations of conductive electrons. These excitations are highly localized and behave, in some ways, similarly to particles. There can be localized surface plasmon-polaritons and propagating plasmon-polaritons [1] which are the result of the relative magnitude of the permittivities of the material at an interface. Detailed derivations of SPPs that result in evanescent waves can be found in a variety of sources

such as [11] but will not be provided here as the plasmons in the simulation result from direct application of the Maxwell equations, the Drude model, and the lasing model which is presented next, not from other external equations or parameters.

4) Lasing and Molecules

To understand the concept of *l*ight *a*mplification by *s*timulated *e*mission of *r*adiation or a laser, three fundamental energy exchange process must be understood – stimulated absorption, stimulated emission and spontaneous emission. Stimulated absorption is perhaps the most intuitive of the three. Consider a molecule in some state. When a photon with the energy equivalent to the difference between the molecule's next energy level and the current state is absorbed by the molecule, the molecule has the energy to vibrate at the next energy level. Stimulated emission is similar but perhaps less intuitive. The molecule, now in the first excited state absorbs another photon of the same energy, but instead of rising in energy to the next level, the molecule re-emits the photon that it absorbed, along with another identical one, falling back down to the ground state. Quantum mechanically, the probability of stimulated emission or absorption happening is identical in this simple scenario [12].

Stimulated emission was first described by Einstein through his famous A and B coefficients. Consider a group of molecules that can be in state a or b. Performing a simple dynamic balance assuming a probability distribution $\rho(\omega_0)$:

$$\frac{dN_b}{dt} = -N_b A - N_b B \rho(\omega_0) + N_a B \rho(\omega_0) \qquad (1.13)$$

where A is the spontaneous emission and B is the stimulated emission/absorption coefficient [12]. Einstein compared the distribution derived from the above equation to the

8

blackbody emission equation and found expressions for A and B. For a system in thermal equilibrium [11]:

$$\frac{stimulated\ emission}{spontaneaus\ emission} = \frac{1}{e^{h\nu/kT} - 1} \tag{1.14}$$

The expressions for spontaneous emission are well-known. It is a well-known result from Quantum Electro Dynamics (QED), such as described in [12] that spontaneous emission is stimulated emission in which the stimulation comes from the vacuum fluctuations. As may have become clear, the method of simulation that will be presented is semi-classical, which is why the Maxwell equations are used. Unless full QED is implemented, spontaneous emission must be simulated somehow. More on this in a bit.

The lasing model used in this work consists of a four-level molecule formulation. Consider a molecule with 4 distinct energy states, E_0, E_1, E_2, and E_3. The spacing between levels E_3 and E_2 and E_1 and E_0 are small in comparison to E_2 and E_1. The levels will be referred to by their number density, N_i, respectively. Figure 2 shows the rendition that was used in the molecular layer in Figure 1.
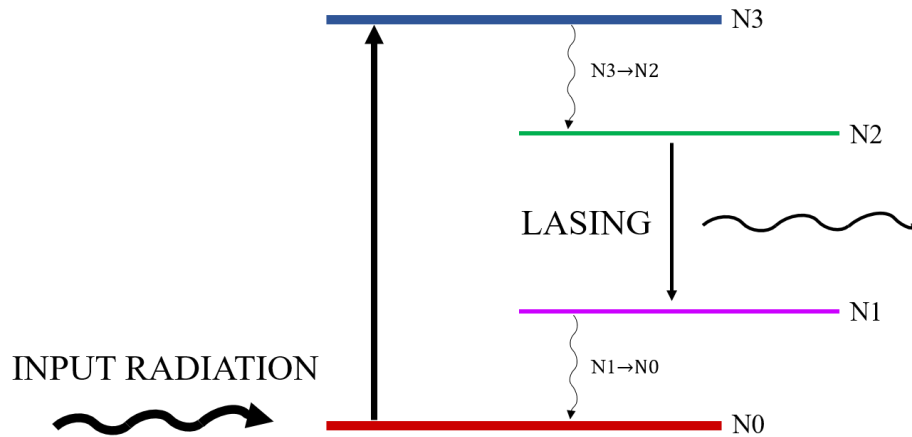
Figure 2: 4-level molecular model. N2 and N1 are considered the lasing levels. Population inversion is achieved when N3 is greater than N1.

The lifetimes of the states N_3 and N_1 are small due to non-radiative decay such as phonon scattering. Coupling this model to an external electromagnetic field, the working equations for the molecules are finally generated:

$$\frac{\partial N_3}{\partial t} = \frac{1}{\hbar \omega_b} \vec{E} \cdot \frac{\partial \vec{P}_b}{\partial t} - \frac{N_3}{\tau_{32}}$$

$$\frac{\partial N_2}{\partial t} = \frac{N_3}{\tau_{32}} + \frac{1}{\hbar \omega_a} \vec{E} \cdot \frac{\partial \vec{P}_a}{\partial t} - \frac{N_2}{\tau_{21}}$$

$$\frac{\partial N_1}{\partial t} = \frac{N_2}{\tau_{21}} - \frac{1}{\hbar \omega_a} \vec{E} \cdot \frac{\partial \vec{P}_a}{\partial t} - \frac{N_1}{\tau_{10}}$$

$$\frac{\partial N_0}{\partial t} = - \frac{1}{\hbar \omega_b} \vec{E} \cdot \frac{\partial \vec{P}_b}{\partial t} + \frac{N_1}{\tau_{10}}$$

(1. 15)

Lasing occurs as a chain reaction. The input radiation or pump stimulates the molecules to the upper most level with a frequency/energy, $\omega_{3 \leftrightarrow 0} = \omega_b = E_3 - E_0$. The molecules at the top level rapidly decay (small τ_{32}) to level N_2. If there were no spontaneous emission, the molecules would just pile up there and nothing would happen. Due to numerical errors, there are tiny amounts of various other frequencies besides the pump frequency that is used. Observe Figure 3 below.
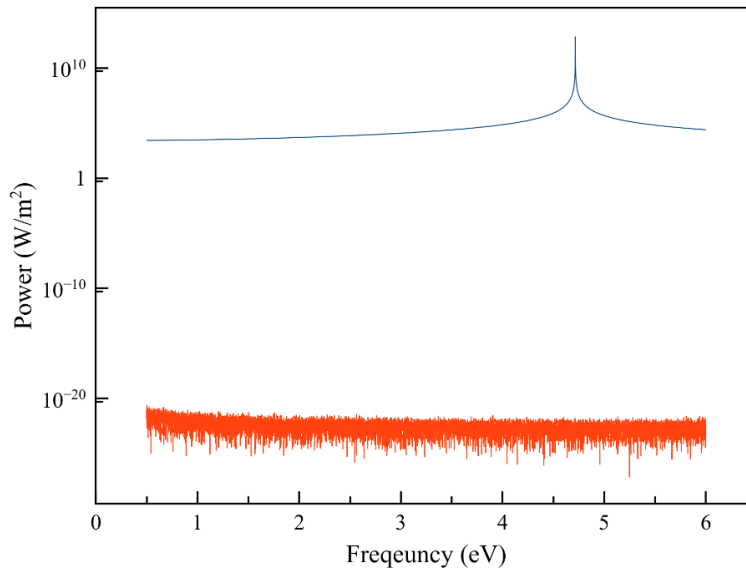
Figure 3: FFT of CW. Blue is the Transmission, Red is the noise floor (the Reflection)

The blue curve shows a CW (continuous wave). The code is set to generate a single sine wave with a frequency of 4.716 eV. A perfect simulation would show a delta spike at 4.716 eV only. Considering the noise floor in red, all frequencies are present at small magnitudes. Because of this, the numeric error can mimic the vacuum fluctuations and stimulate the molecules in N_2 to decay to N_1 by emitting radiation at the lasing frequency, $\omega_{2\leftrightarrow1} = \omega_a = E_2 - E_1$. Molecules at N_1 decay rapidly as well via small τ_{10}. The equations that are used in the simulations have now been generated as equations 1.8, 1.12 and 1.15.

D. Yee's Algorithm

The Yee algorithm, developed by Kane Yee in 1966 is the method of choice for high level, computation optics simulations. Of course, numerical methods must be used in a computation setting. For example, using the Finite Difference Time Domain for the following equations:

$$
\begin{aligned}
\frac{\partial E_y}{\partial x} - \frac{\partial E_x}{\partial y} &= -\mu_0 \frac{\partial H_z}{\partial t} \\
\frac{\partial H_z}{\partial y} &= \sigma E_x + \epsilon \frac{\partial E_x}{\partial t} \\
\frac{\partial H_z}{\partial x} &= -\sigma E_y - \epsilon \frac{\partial E_y}{\partial t}
\end{aligned}
\tag{1.16}
$$

Converting them to their numerical approximations:

$$
\begin{aligned}
\rightarrow \frac{E_y(i+1,j)-E_y(i,j)}{\Delta x} - \frac{E_x(i,j+1)-E_x(i,j)}{\Delta y} &= -\mu_0 \frac{H_{z,t}(i,j)-H_{z,t-1}(i,j)}{\Delta t} \\
\rightarrow \frac{H_z(i+1,j)-H_z(i,j)}{\Delta y} &= \sigma E_x(i,j) + \epsilon \frac{E_{x,t}(i,j)-E_{x,t-1}(i,j)}{\Delta t} \\
\rightarrow \frac{H_z(i,j+1)-H_z(i,j)}{\Delta y} &= -\sigma E_y(i,j) - \epsilon \frac{E_{y,t}(i,j)-E_{y,t-1}(i,j)}{\Delta t}
\end{aligned}
\tag{1.17}
$$

11

Yee brilliantly realized that if the electric field and the magnetic field were put on interlocking grids, the equations would be explicitly solvable in the above form. The grid used is visualized in Figure 4. The curls needed are easily seen around each vertex of the cubes in c).
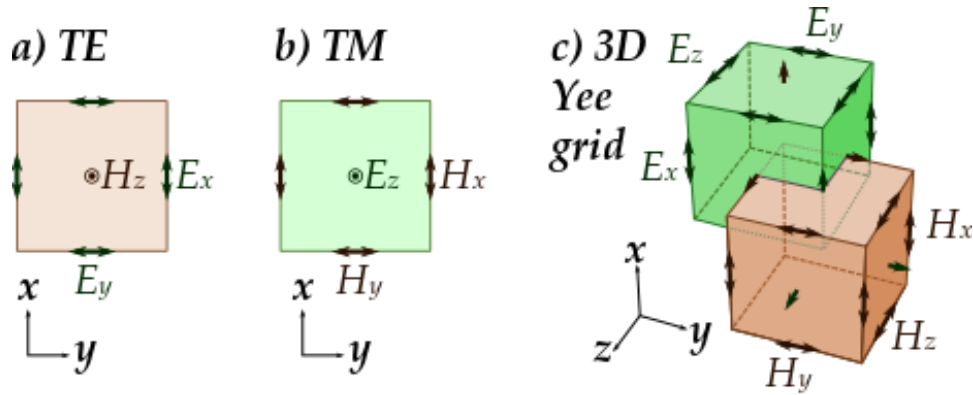
Figure 4: Visualization of Yee's Algorithm. Note the interlocking grid from which the curl is immediately obvious. Creative Commons Copyright.

In addition to its ease, the Yee algorithm has several advantages including implicit use of boundary conditions just by the setup of the simulation [10]. The code is then written to create the interlocking grids. In vacuum, the Maxwell equations are used alone. In metal or molecules, the Maxwell equations are used in conjunction with either the Drude model or the Population model, respectively.

II. PLASMON SYSTEM

A. Plasmon Resonance

To provide the strongest coupling between the metal *Plasmons* and the molecular layer, the system was first simulated without molecules. A series of tests were conducted to observe the frequency response of the transmission and reflection when the silver slits were

stimulated by an electric field pulse with a variant of a Blackman-Harris line shape for various geometries:

$$E(t) = E0 \times \cos(\omega t) \times \left(a_0 - a_1 \cos\left(\frac{2\pi t}{\tau}\right) + a_2 \cos\left(\frac{4\pi n}{\tau}\right) + a_3 \cos\left(\frac{6\pi n}{\tau}\right) \right) \qquad (2.\ 1)$$

In which a_0, a_1, a_2, and a_3 where set to produce a large amount of stimulating frequencies. The transmission (Tr), reflection (Re), and absorption (Ab) of the slits given as normalized fractions are then observed. Of course, as energy is conserved:

$$Ab = 1 - Tr - Re \qquad (2.\ 2)$$

Nine geometries were tested. The transmission results are given in Figure 6 and Figure 5. As the molecular sheet in subsequent tests is placed on the transmission side of the system, the resonant frequency of the transmission is frequency of interest. For increasing t and decreasing R, there is a redshift in resonance as the respective dimensions are increased. Interestingly, there does seem to be a threshold for resonance for the parameter t.
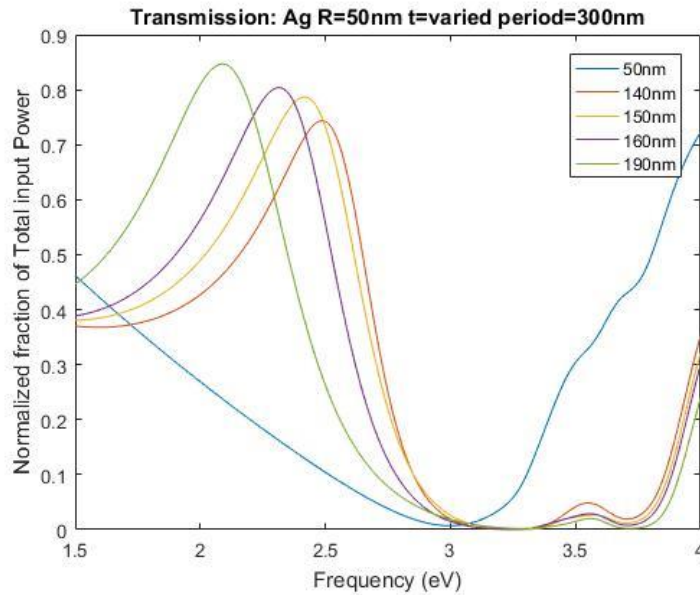
Figure 5: Transmission Frequency Response of Ag silts of various geometries, varying t-parameter

13
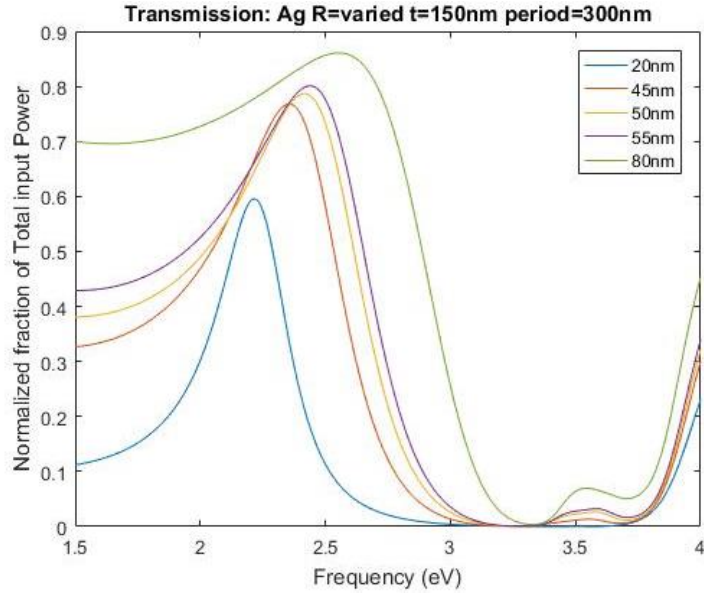
Figure 6: Transmission Frequency Response of Ag silts of various geometries, varying R-parameter

B. Molecular Simulations

Due to the time involved in collecting data, and, as will be shown in the remainder of this section, the volume of data that was collected and processed for one specific geometry, only one silver-slit geometry – $R = 45nm$ and $T = 150nm$ – was used. The resonant Plasmon frequency of this geometry, as determined in the previous section, is $\omega = 2.358 \, eV$. The primary system parameters that were changed during tests where the number density of the molecules (nD), the molecular thickness (Mt), and the input electric field amplitude (E_0).

1) A note on Transient Responses

As a caution to other researchers in this field – transience can be difficult to determine. From previous experience, the number of time steps was originally set to 4 million, which was thought to be sufficient to reach a steady state. This assumption yielded spectra with general shapes resembling the following:

14
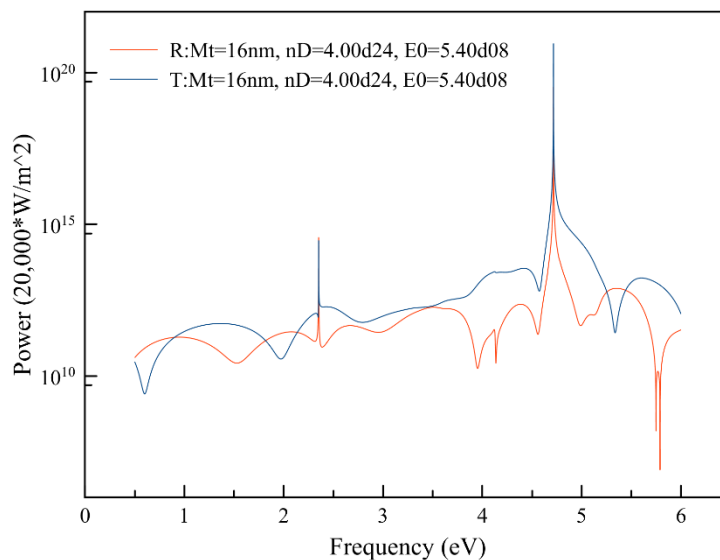
Figure 8: Standard geometry with FFT over complete 10 ps simulation.

Originally it was assumed that these were in steady state; however, by just sheer curiosity, the number of time steps was increased to 8 million and the same spectra came out like in Figure 7.
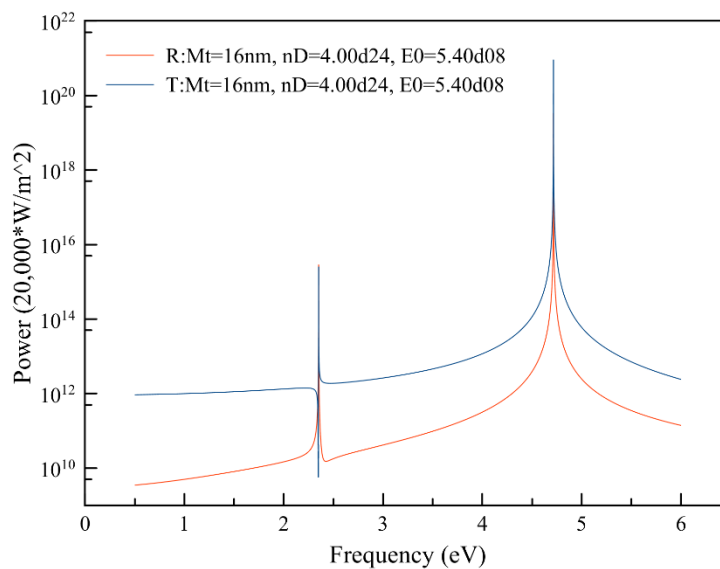
Figure 7: Standard geometry with FFT over 10 ps after initial 10 ps simulation.

15

Only after analysis of the molecular populations does this behavior become clear. Without analysis of molecular population densities, the researcher is somewhat in the dark as to when to begin taking the FFT. As will be shown however, there is generally little to no qualitative behavior loss. Much of the analysis in the following section will be done using responses containing transience as this was not discovered till later in analysis. One battery of simulations was conducted without transience, the similarities and differences of which are noted in Section II-B3.

2) FFT Results

FFT analysis was conducted to explore the effect the molecular layer thickness, the molecular density, the input electric field frequency, and the input electric field intensity on the lasing response of the system. The original system that was tested was the $20\ nm$ system with a molecular density of $4{\times}10^{24}\ \frac{molecules}{m^3}$ with a total of 4 million time steps for a total of $10\ ps$, during which FFT was conducted throughout.
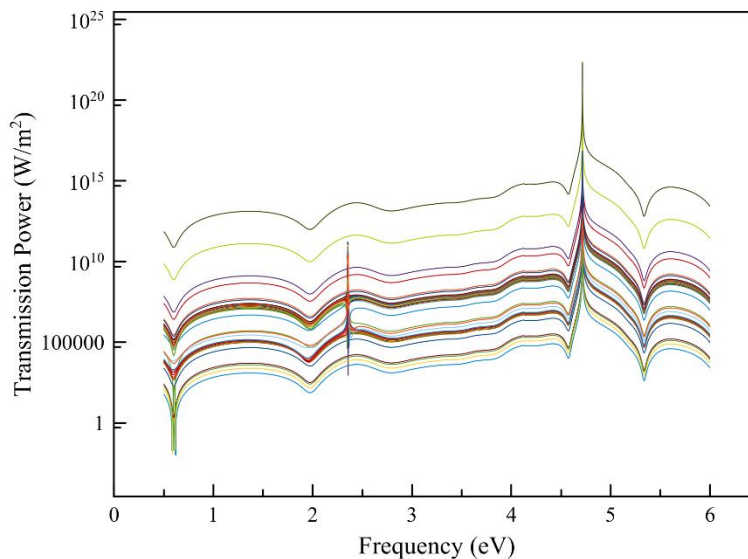
Figure 9: Complete Transient FFT spectra for Mt = 20nm, varying E0 from $1.00d7\ \frac{v}{m}$ to $1.00d9\ \frac{v}{m}$

16

The spectra are graphed on top of each other showing the relative power increase as input power increased in Figure 9. The transient signatures in each of the spectra can be observed. The excitation peak at 4.716 eV is due to the pump input. The lasing peak can be observed in some of the spectra around the expected 2.358 eV. In Figure 10, the spectra are graphically separated to demonstrate more subtleties of behavior. On the left, the range of E0 is $5.10d8\frac{v}{m}$ to $7.00d8\frac{v}{m}$ from left to right and on the left the range of E0 is $9.00d7\frac{v}{m}$ to $3.00d7\frac{v}{m}$ from left to right.

Figure 10: The left figure shows the transient Mt=20nm spectra from E0 $5.10d8\frac{v}{m}$ to $7.00d8\frac{v}{m}$ spaced out to see the decrease and disappearance of the lasing peak. The right figure shows the spectra from E0 from $9.00d7\frac{v}{m}$ to $3.00d7\frac{v}{m}$ spaced out to see the appearance and increase of the lasing peak.

The appearance and increase in amplitude of the lasing peak can be seen on the right and the decrease in amplitude and subsequent disappearance of the peak can be seen on the left. Closer details of the above spectra are given in the Appendix, Figure 52 and Figure 53. Some of the spectra have Fano-resonances, some are seen to contain minute numerical graininess, and the transient signatures are apparent; however, what is most interesting is the rather sudden appearance and disappearance of the lasing peak. Spectral data as

contained in the above figures was likewise generated for various Mt and nD as functions of varying $E0$, the analysis of which is given in the following section. After it was realized that the "texture" in the above spectra was due to transience, the Mt tests were conducted again. For comparison, the "revised" system that was tested was the $Mt = 20\ nm$ system with a molecular density of $4 \times 10^{24}\ \frac{molecules}{m^3}$ with a total of 8 million time steps for a total of $20\ ps$, during which FFT was conducted throughout the final $20\ ps$. The difference between Figure 9 and Figure 11 is dramatic – the spectra are now incredibly smooth out side of the pump and lasing peaks.
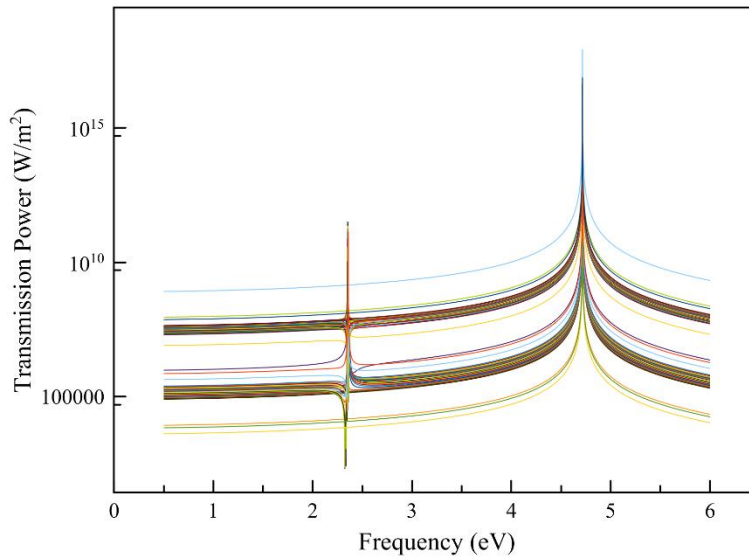
Figure 11: Complete Revised FFT spectra, varying E0 $7.00d6\frac{v}{m}$ to $3.00d9\frac{v}{m}$

Closer details of the Figure 12 are given in the Appendix, Figure 54 and Figure 55. Contrasting with the transient response, the smoothness of the spectra is evident; however, the sudden appearance and disappearance of the lasing peak remains unchanged.
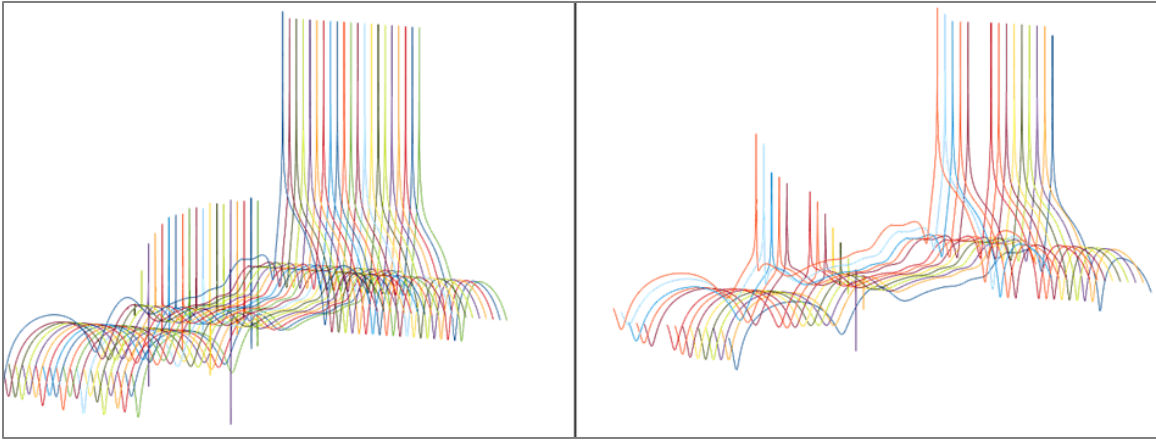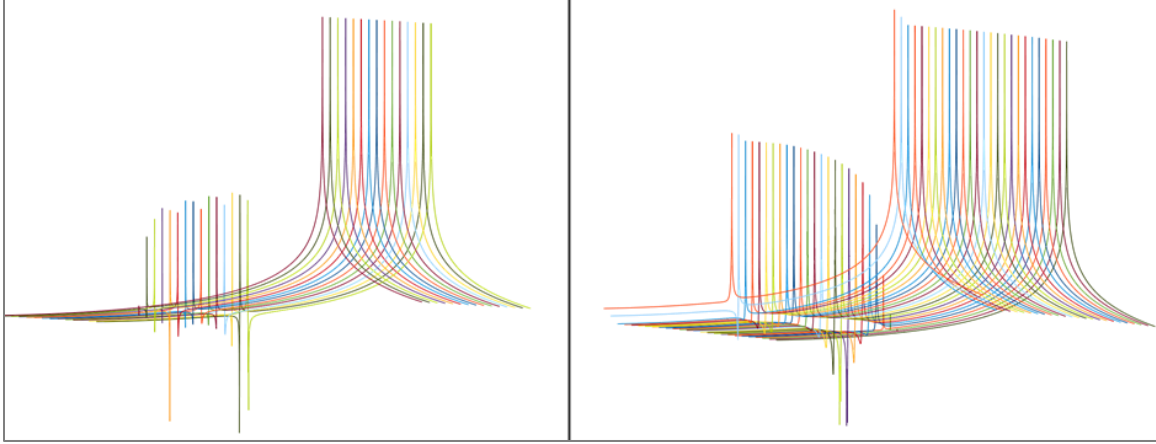
Figure 12: The left figure shows the revised Mt=20 nm spectra from E0 from $7.00d8\frac{v}{m}$ to $5.60d8\frac{v}{m}$ spaced out to see the decrease and disappearance of the lasing peak. The right figure shows the spectra from E0 from $9.00d7\frac{v}{m}$ to $3.00d7\frac{v}{m}$ spaced out to see the appearance and increase of the lasing peak.

Even with the care taken to get numerical convergent results, the extreme nature of the plasmon-molecule system is such that there are still numerical issues. This is evident in Figure 56 given in the Appendix, which gives the detail of four of the spectra from the above figure. Even though the graininess is not extreme enough to pose a problem, it must be noted and kept in mind during further analysis.

The similarities and differences will become more clear in the following section but although the quantitative realization of the transient and revised results is different, the qualitative results seem to match. This assumption is only partially valid. The transient spectra, given in Figure 14, of the $15\ nm$ system with a molecular density of $4\times10^{24}\frac{molecules}{m^3}$ with a total of 4 million time steps for a total of $10\ ps$, during which FFT was conducted throughout.. These transient spectra show no signs of a lasing peak. However, the $15\ nm$ system with a molecular density of $4\times10^{24}\frac{molecules}{m^3}$ with a total of

19

8 million time steps for a total of $20\ ps$, during which FFT was conducted throughout the final $20\ ps$ has the following behavior, given in Figure 13 does show lasing.
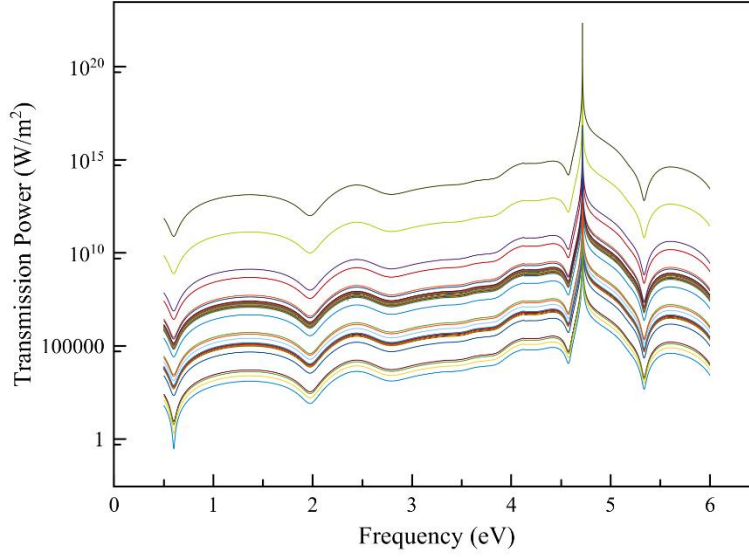
Figure 14: Complete Transient FFT spectra for Mt=15nm, varying E0 from $5.00d6\frac{v}{m}$ to $5.00d11\frac{v}{m}$
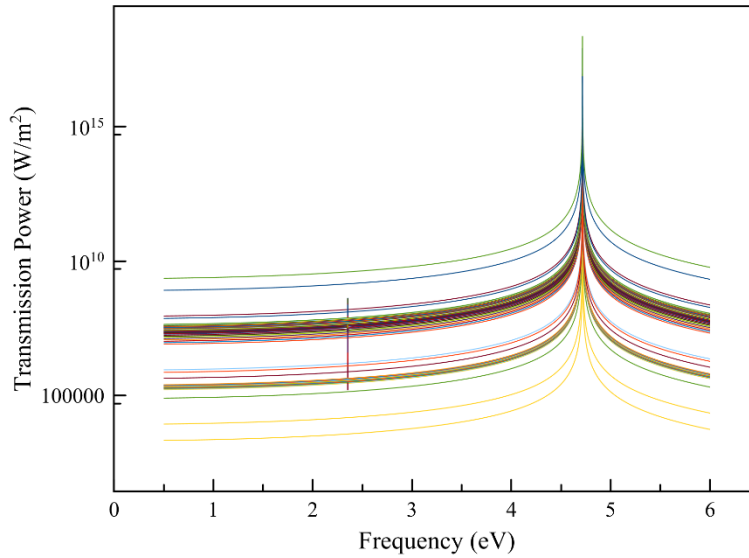
Figure 13: Complete Revised FFT spectra for Mt=15nm, varying E0 from $5.00d6\frac{v}{m}$ to $5.00d9\frac{v}{m}$

If the lasing section of Figure 13 is zoomed in:
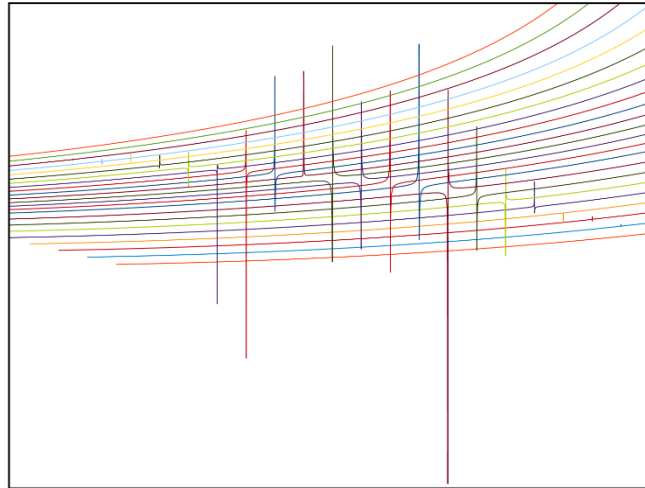
Figure 15: Zoomed in portion of 15nm spectra detailing the lasing section

There is lasing. the problem with the transient spectra is that the time in which lasing manifests itself is roughly at 10 ps as will be shown in Section II-C2. In the case of the 15nm, the lasing is quite weak and is not able to show up in the transient response. In the case for the 20nm, the lasing was stronger and could be detected in the FFT in the transient response. Therefore, the transient response gives an attenuated idea of the full dynamics of the system. Similar figures are given in the Appendix for a system with Mt = 30nm for completeness. The same behaviors as in the Mt = 20nm case are observed.

3) FFT Analysis and The Lasing Profile

To clearly see the effects that the various parameters have on the lasing response of the system, the need for a more convenient method of analyzing the FFT spectra is apparent.

Concentrating on the lasing peak and recalling that there is still some numerical graininess, the following algorithm is used:

1. a peak search in the 0.500 to 3.000 eV range finds the frequency of the highest point (if there is no peak, this corresponds to the 3.000 eV frequency) per spectra.

2. This is conducted for all spectra of a specific nD and Mt and gathered into a peak frequency out vs. input power

3. A numerical integration is calculated between 2.3499 to 2.3702 eV to gather to minimize effects of the graininess per spectra.

4. This is conducted for all spectra of a specific nD and Mt and gathered into a power output vs. power input.

The result of 2 shows the frequency dependence on input power and the result of 4 is termed the "lasing profile". The lasing profile is something that is not used in the literature, with the signature of lasing being reserved to the lasing peaks demonstrated in the previous section. Although the lasing profile does not technically generate any new information, it does have the advantage of clearly demonstrating the characteristic threshold and saturation responses of a lasing system. Taking the original system that was tested was the $20\ nm$ system with a molecular density of $4\times10^{24}\ \frac{molecules}{m^3}$ with a total of 4 million time steps for a total of $10\ ps$, during which FFT was conducted throughout and running it through the above algorithm:
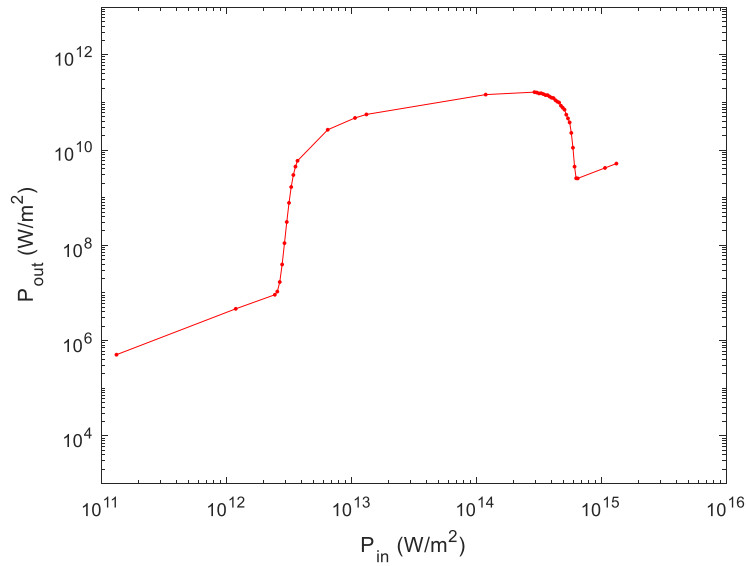
Figure 16: Total Transmission Power between 2.3499 to 2.3702
eV for nD=4d24 and Mt=20nm vs. Input Power

Just given in Figure 16, clearly, there is a "region of interest" in the middle that exists. The

equation below gives the power law dependence which will be referred to from time to

time:

$$n = \frac{\log P_{out,final} - \log P_{out,intial}}{\log P_{in,final} - \log P_{in,intial}} \tag{2.3}$$

where n is the power-dependence. If this equation is applied to the "linear" regions, a value

of $1 \pm 0.9\%$ (depending on which points are used) is obtained. Applying the above

equation to the profile with the initial and final values being the closet data points, an

estimate for the power law throughout the profile is obtained.

23
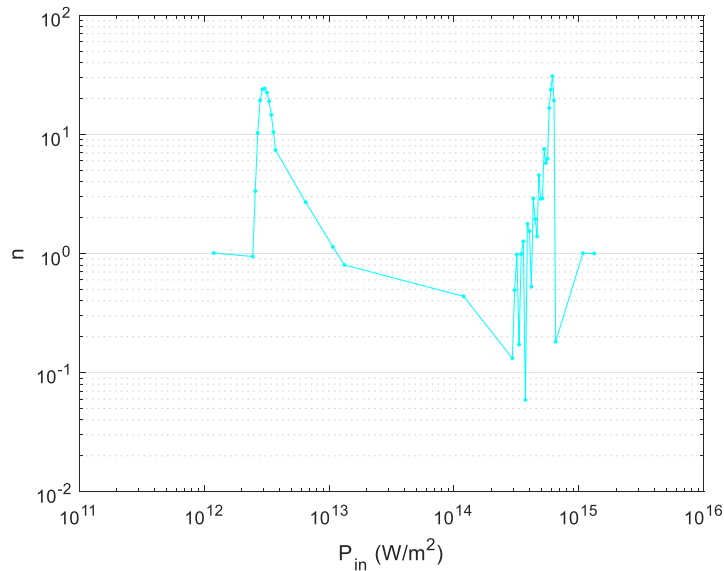
Figure 17: Power Law exponent as a function of input power, absolute value

The absolute value was taken to place the data in a log scale. Notice that there is some noticeable symmetry (of course the second half of the graph is negative). The two regions in Figure 16 where the output power is suddenly far greater correspond to the two spikes in Figure 17 in which the $n \approx 30$. These regions are what are referred to as the lasing threshold and saturation regions, respectively. The lasing peaks in the FFT spectra appear/disappear in these regions, before there is a pre-threshold, post-saturation, and in-between, there is, to an approximation, a linear dependence on input power.
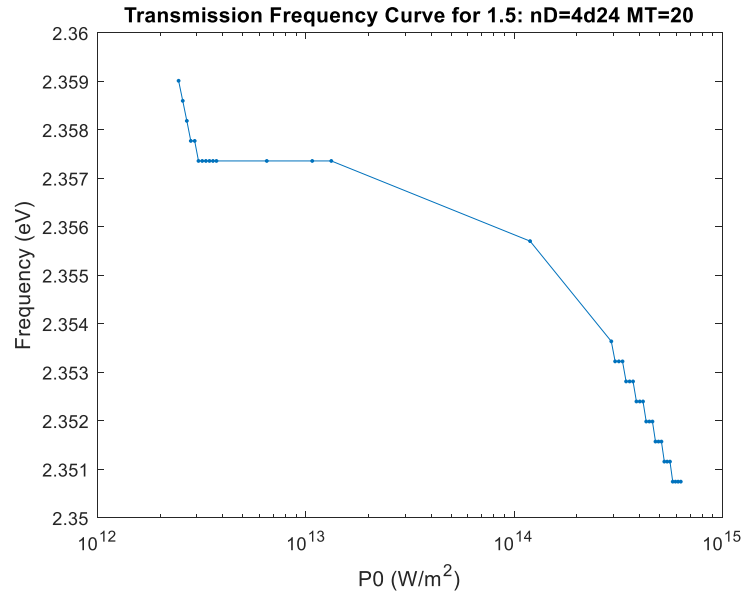
Figure 18: Peak Frequency as a function of input Power

Figure 18 shows the behavior of the lasing peak frequency. Notice, the frequency does not change by much, however there is a definite decrease as a function of input power. This is the standard behavior for all the lasing profiles. Since the lasing profile was most finely determined for $Mt = 20nm$ in both the transient and revised data, only in those analyses will the power law functionality be demonstrated. The above lasing profile was for a specific geometry of the lasing system. In the transient data, quite a few geometries were investigated. In the Figure 19 below, the lasing profiles of the system with increasing molecular thickness are overlaid on one another.
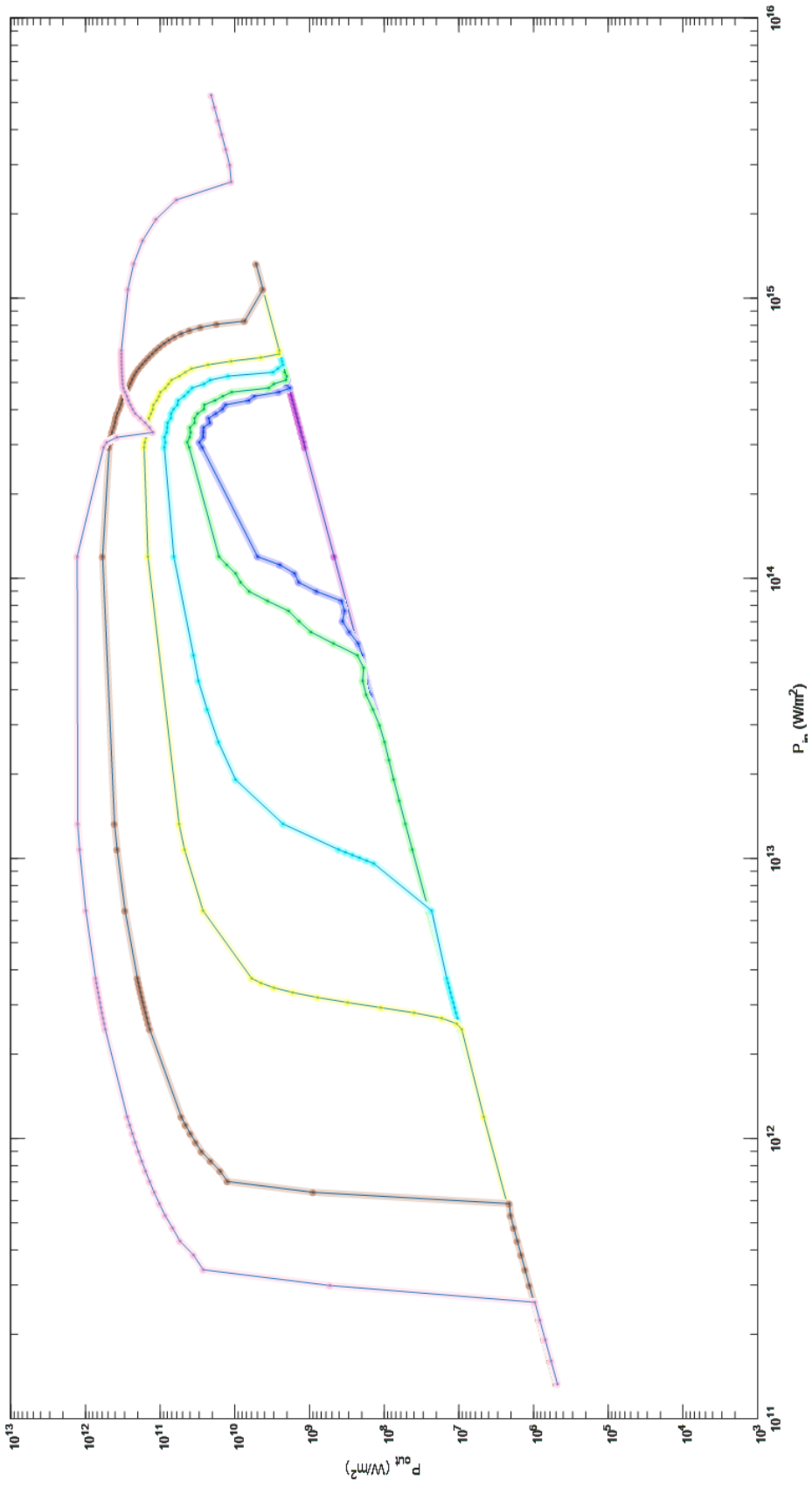
Figure 19: Lasing Profiles varying in Mt. Purple: 15nm | Blue: 16nm | Green: 17nm | Cyan: 18nm | Yellow: 20nm | Brown: 30nm | Pink: 60nm

As the molecular thickness is increased, the lasing profile gets larger, both in the input powers in which lasing can occur – threshold decrease and saturation increase, and in the output powers. The lasing threshold gets steeper as the molecular thickness increases. The notch in the 60 nm lasing profile is a numerical artifact due to the size of the simulation space. Lasing profiles with $Mt >$ $60nm$ will have the same notch. Figure 64, given in the Appendix, shows the lasing profile as a function of molecular density. The profile increases in width and height with increasing density. Numerical stability seems to be a problem for $nD = 5.0d24$ due to the small peaks at the end of the saturation region. Also, given in the Appendix, Figure 65 shows the lasing profile as a function of the detuning. The $\omega_{2\leftrightarrow1}$ value refers to the transition frequency of the molecules from n2 to n1. There is a very small window of frequency detuning between the Plasmon resonance and the molecular transition frequency of approximately $\pm2\%$ of the plasmon resonance frequency. Interestingly, the largest lasing profile did not occur at perfectly matching frequencies, it seems that slight detuning towards the blue frequencies is favorable. Finally, the same procedure was conducted for the revised data with the longer simulation time, shown in Figure 20. The behavior of the lasing profiles for the transient and revised data is the same. The difference is that the transient lasing profiles are smaller in every respect. This confirms that the qualitative aspects of the transient profiles are useful.
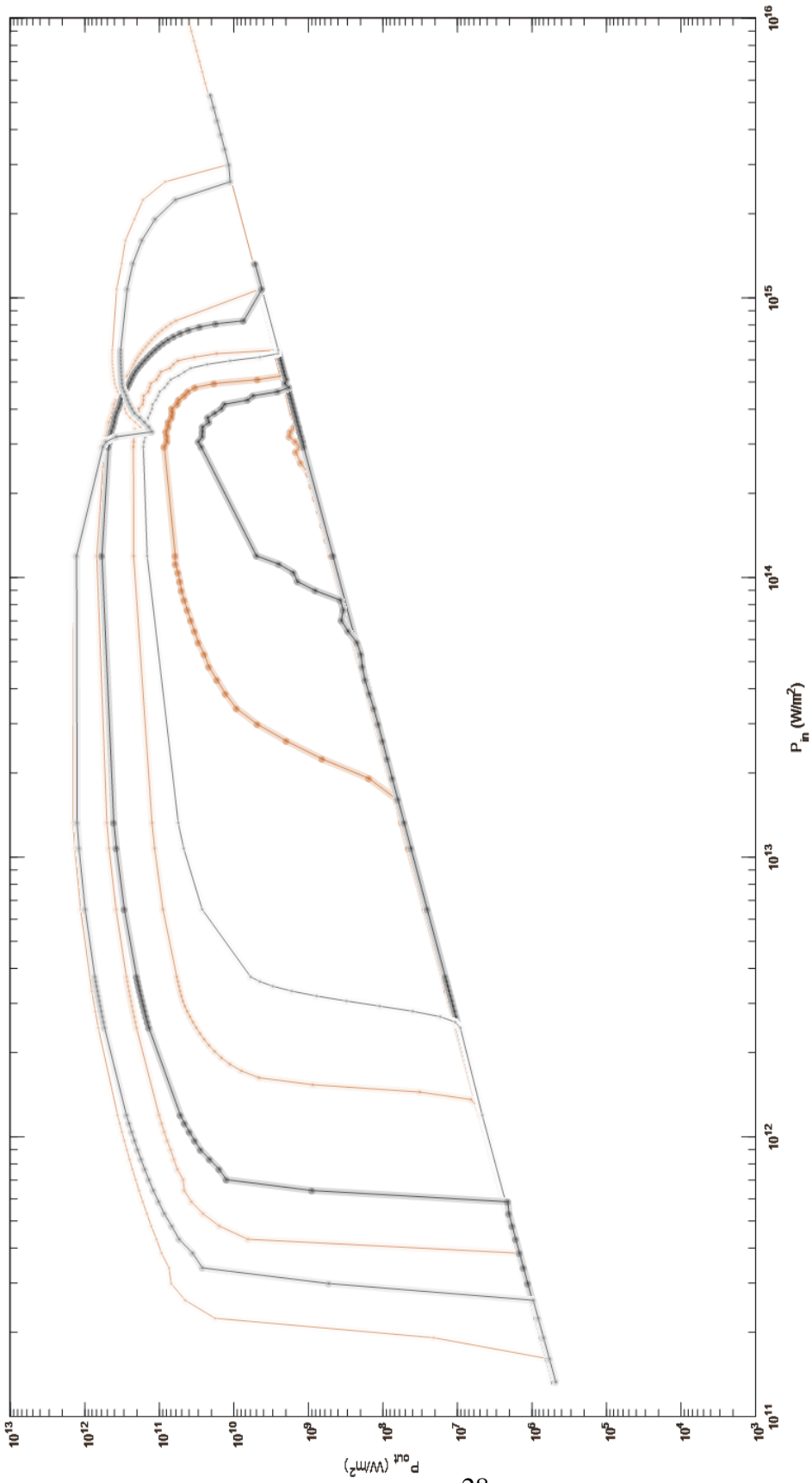
Figure 20: Comparison between the transient and revised lasing profiles. The gray curves correspond to the transient responses and the orange the revised. The sequence of Mt is identical for both: 15nm, 16nm, 20nm, 30nm, 60nm.

4) Super-florescence

An interesting phenomenon that was tested was that of super-florescence. The system that was tested was the $20\ nm$ system with a molecular density of $4\times10^{24}\ \frac{molecules}{m^3}$ with a total of 4 million time steps for a total of $10\ ps$, during which FFT was conducted throughout; but, instead of the molecules starting in the ground state n0, the molecules are started in the lasing excited state, n2. The same pulse with the Blackman-Harris window of equation 2.1 that was used in Section II-A was sent through the system. The pulse would theoretically simulate a spontaneous emission, which would set off the lasing chain reaction. However, the pulse is short, and there would be no pump source to continue the lasing cycle, so there would just be a lase pulse. This phenomenon was observed over several molecular densities. For relatively low densities:
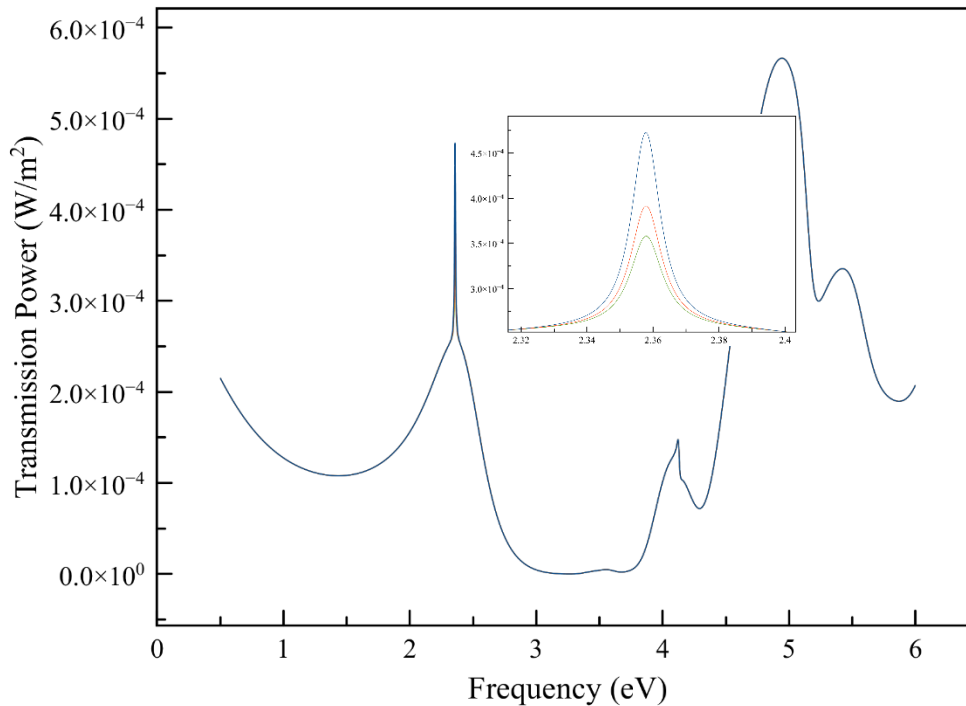
Figure 21: Transmission Frequency Response of Superfloresent system. Inset shows detail at 2.358 eV: nD = Green: 4d23 | Red: 5d23 | Blue: 7d23

29

All the tests were stimulated by a pulse amplitude $E0 = 1d4\frac{V}{m}$ and a central frequency of $\omega = 2.358$, only the molecular density was changed.
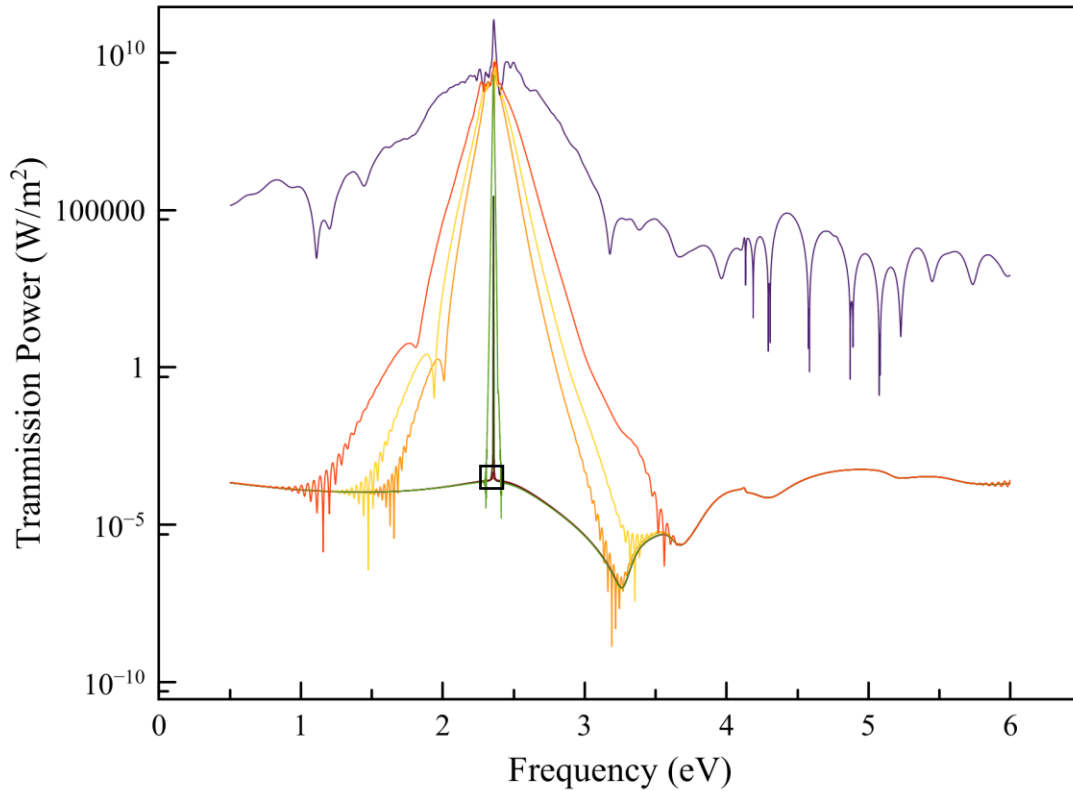
Figure 22: Transmission Frequency Response of Super-florescent system. Black square gives the location of inset in Figure 21. nD = Brown: 5d24 | Green: 7d24 | Orange: 4d25 | Yellow: 5d25 | Orange: 7d25 | Purple: 4d26

As the molecular density of the system is increased, the lasing peaks grow because there is, effectively, more energy in the system. Considering the molecules to each "contain" the lasing photon, as the number of molecules is increased, the total number of photons that can be emitted is increased. The peak widens and starts demonstrating other resonances as

30

the density is increased. This due to the increasing internal reflections and resonances that are formed within the molecular layer. Especially for $nD = 4d26$, these resonances and reflections become so great that the spectrum looks like a mess. Since there is no steady state achieved as the system is purely dissipative, this simple example demonstrates why there was such a difference between the transient and revised spectra in Section II-B2.

5) Separation

The molecular layer was separated from the silver slits to test the localization of the plasmons. The system that was tested was the $20\ nm$ system with a molecular density of $4 \times 10^{24} \frac{molecules}{m^3}$ with a total of 4 million time steps for a total of $10\ ps$, during which FFT was conducted throughout.
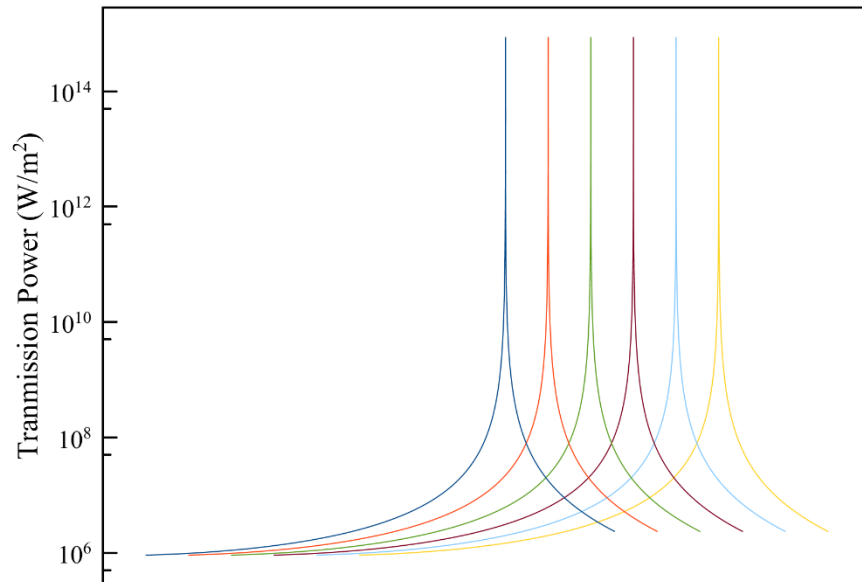
Figure 23: The Transmission Power Response of the system in which the molecular layer was separate by 1nm, 5nm, 10nm, 20nm, 30nm, and 40 nm. None are labeled as the response were identical. The spectra are spread out over the x-axis to demonstrate that they are identical. The peaks are each at 4.716 eV.

6) No-metal

Finally, the system with the $20\,nm$ thickness and a molecular density of $4 \times 10^{24}\,\frac{molecules}{m^3}$ with a total of 4 million time steps for a total of $10\,ps$, during which FFT was conducted throughout was run but without the silver slits, just the molecular layer. Since there are no plasmons, this test would confirm that the presence of plasmons influences the lasing capabilities of the system.
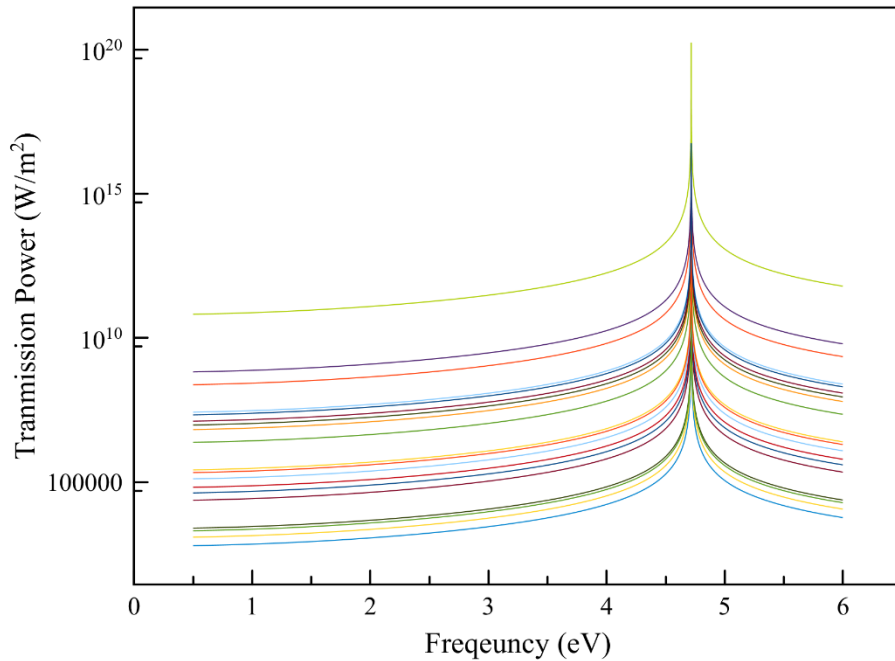
Figure 24: Transmission Spectra of the molecular system without the silver slits over same E0 range as in Figure 9 and Figure 11. No lasing is observed.

An attempt was made to see when/if lasing occurred at even higher input electric field amplitudes. With the time and spatial resolutions used in the code, $E0 > 5d11$ where uncalculatable. To ensure numerical convergence would involve reducing the grid and generating far more memory and time requirements. Regardless of whether the localized

intensity of the plasmon resonance or something related to reflections and energy transfer back and forth, it is obvious that the plasmons are necessary for lasing to occur within the given parameters.

7) Summary

The work presented in the previous sections was plentiful. A summary of the most important/interesting findings is in order.

1. For a CW stimulation of a lasing system, there is a transient period. This must be considered when spectra are reviewed. Unfortunately, via spectra analysis alone, there is no way to determine the transient period before tests are conducted.

2. The existence of a lasing region with relatively sharp threshold and saturation regions was confirmed for a variety of system parameters.

3. The "lasing profile" was presented and shown to be a useful analytical tool to observe phenomenological behavior of a lasing system.

4. The effect of plasmons on lasing was demonstrated in the following ways:

    a. The range of frequency detuning between the lasing frequency and the Plasmon resonance in which lasing could occur was shown to be $\approx \pm 2\%$.

    b. The elimination of the plasmons entirely made lasing impossible over testable range

C. Populations Analysis

Through the above analyses, the effect of the plasmons is apparent, by (lowering the input power needed to achieve lasing for the molecular system). However, the exact behavior of the lasing profile is still hidden. To attempt an understanding of why exactly lasing occurs and see how that lines up with the explanation given in Section I-C4, the

33

behavior of the population densities of each energy level were examined in various ways. As far as the author is aware, this is the first analysis of its kind and has revealed some fascinating phenomenology, which is still under investigation.

1) Terminal Behavior

Of initial interest was to confirm that, indeed, lasing happens under the condition of population inversion as discussed in the introduction. This was done by running a simulation (a single point on a lasing profile) and recording the final population distribution at the end of the simulation. What will be shown are the results from the $20 \, nm$ system with a molecular density of $4 \times 10^{24} \frac{molecules}{m^3}$ with a total of 8 million time steps for a total of $20 \, ps$, the population distribution which is recorded at the last time step. Figure 25 shows the population distribution for an input parameter of $E0 = 1.00d7 \frac{V}{m}$, well below the threshold region. Notice that there is no population inversion. The "lasing level" N_2 greater than the ground state (N_0).

Figure 25: Terminal Population Distribution. Slits are located at $y = 0$ and the center of the slit is at $x = 100$. n0 = Blue | n1 = Yellow | n2 = Green | n3 = Red, for 20nm system with nD=4d24 and E0=1d7 (pre-threshold region on lasing profile)

Figure 26: Terminal Population Distribution. Slits are located at $y = 0$ and the center of the slit is at $x = 100$. n0 = Blue | n1 = Yellow | n2 = Green | n3 = Red, for 20nm system with nD=4d24 and E0=1d8 (central lasing region on lasing profile)

35

Figure 27: Terminal Population Distribution. Slits are located at $y = 0$ and the center of the slit is at $x = 100$. n0 = Blue | n1 = Yellow | n2 = Green | n3 = Red, for 20nm system with nD=4d24 and E0=1d9 (saturation region on lasing profile)
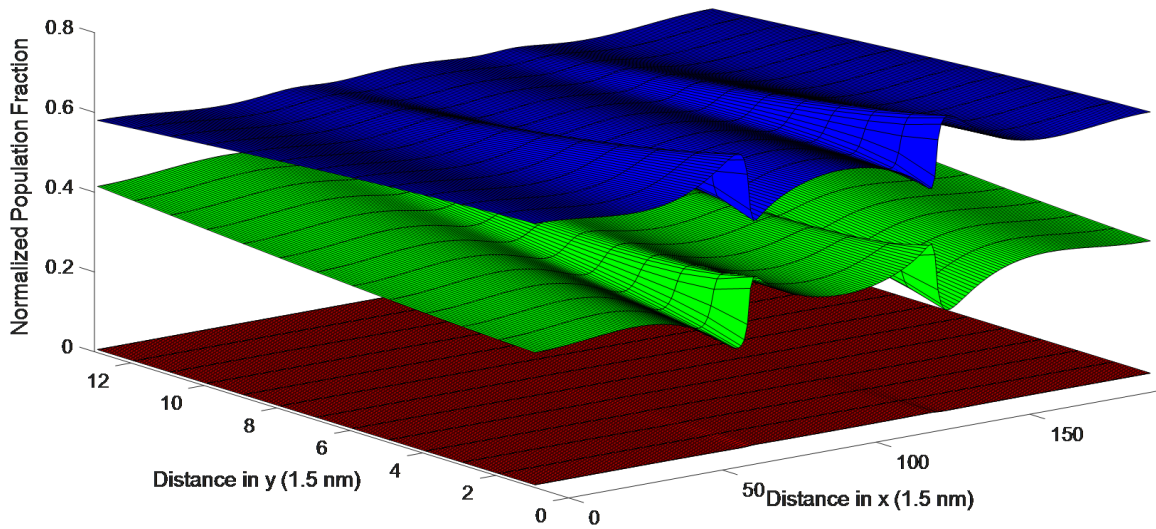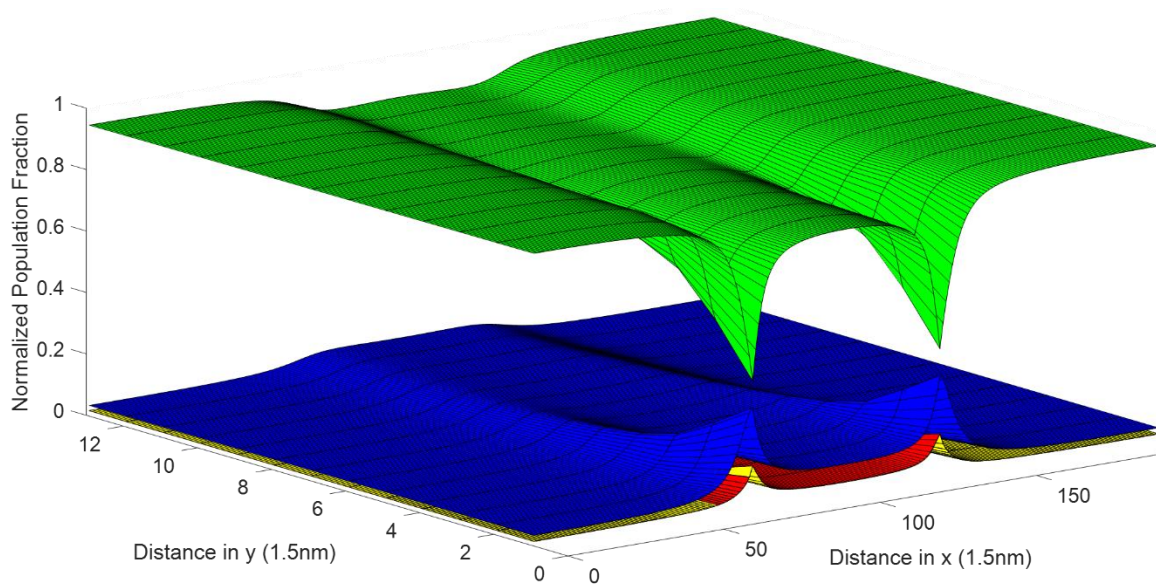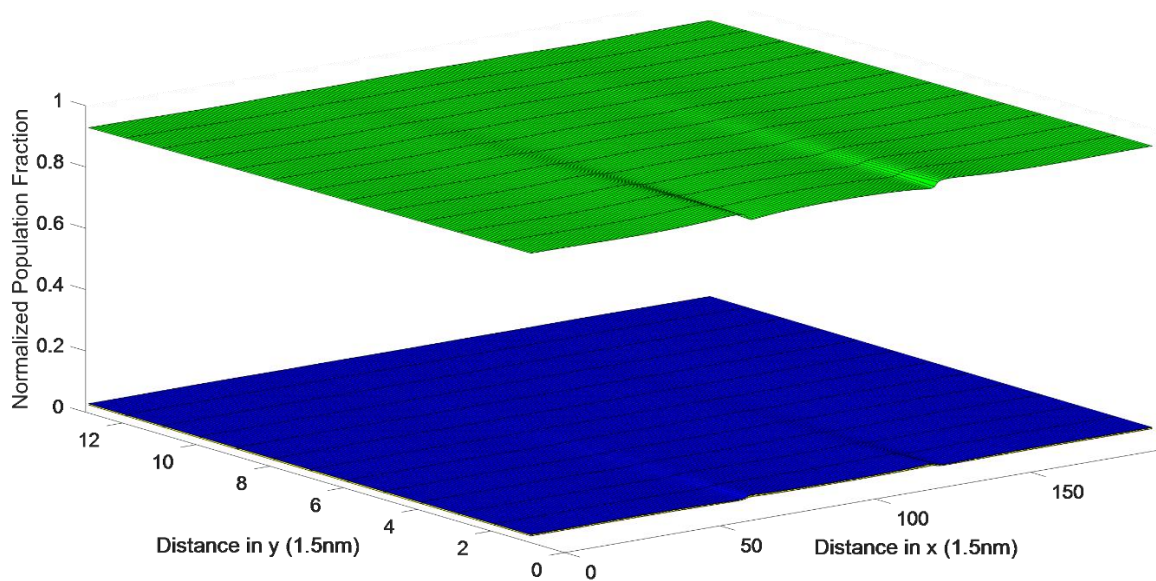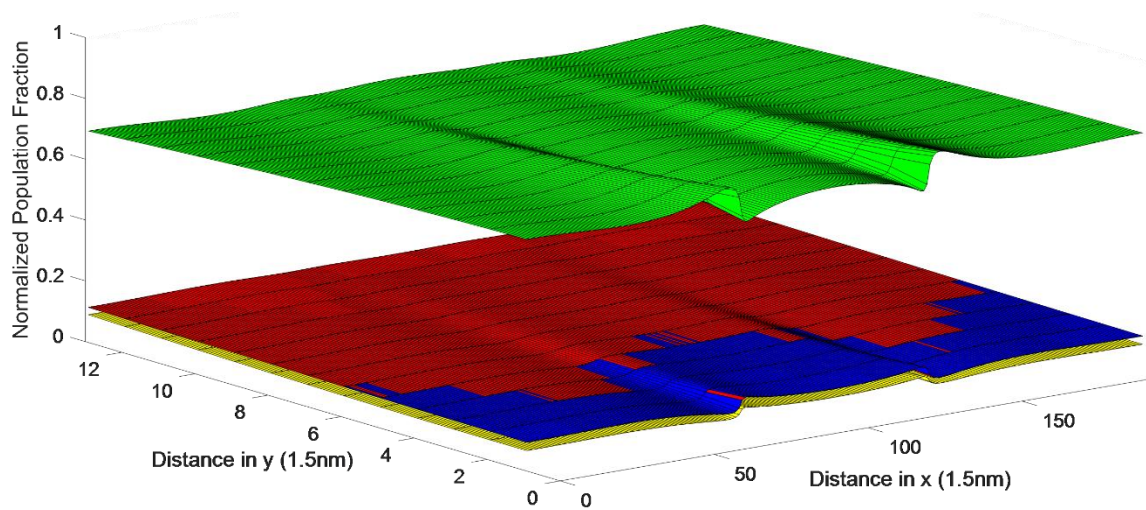

Figure 28: Terminal Population Distribution. Slits are located at $y = 0$ and the center of the slit is at $x = 100$. n0 = Blue | n1 = Yellow | n2 = Green | n3 = Red, for 20nm system with nD=4d24 and E0=3d9 (further saturation region on lasing profile)

Figure 26 shows the terminal response within the lasing region. Note the that there is population inversion. Note, as well, that in the small portion shown, N_1 and N_4 are not consistently one over the other. Figure 27 shows the terminal response in the saturation region. Notice that there is still population inversion. Figure 28 shows the terminal response for an input even further from the lasing region than in Figure 27. The density of N_2 decreased as the input power increased. Also, the density of N_4 surpassed that of N_0 and N_2 is visible.

Various terminal analyses were conducted for several molecular thicknesses. The general patterns presented in the previous figures were followed, however the specific distributions of N_1 and N_3 especially were not consistent. This behavior suggested that either the system had not reached a steady state (which would seem unlikely due to the FFT spectra), or that the system was in an oscillatory equilibrium, and that the terminal analysis, had captured that equilibrium at various points within the oscillations.

2) Selected Dynamic Behavior

The above analysis was conducted due to the initial visualization of the system when lasing. After the terminal analysis did not show a uniformity in region distributions, more out of curiosity than realization, scripts where written that would take record the population distributions at set time intervals during the simulation. Due to memory and time considerations, 500 evenly spaced recordings were made for 12 different parameter settings. Videos were made to make the visual processing easier. Now, the videos, although aesthetically interesting, are not informative, beyond that in which they demonstrated the following two things:

1. What appeared to be some oscillatory behavior during lasing

2. And, when lasing was present, a "state" change which is depicted in Figure 29 would occur
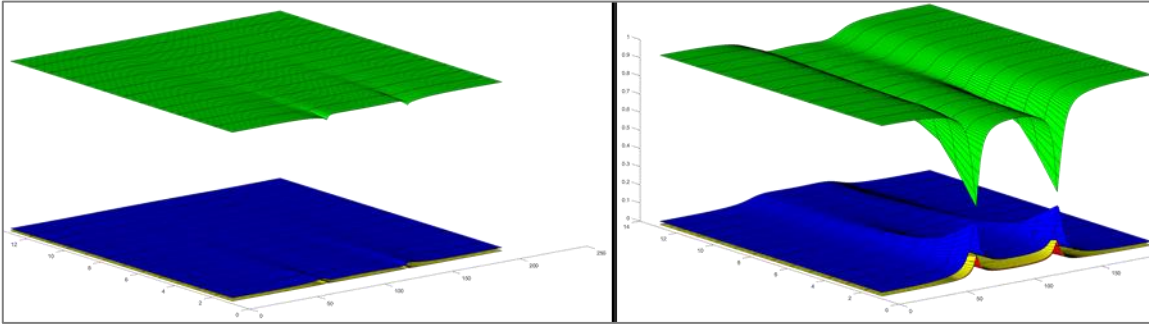
Figure 29: Population distributions at different time steps showing "change of state" that occurs after which the FFT is performed. On the left the time step is 1952000 and on the left is 2400000, both out of 8000000. n0 = Blue | n1 = Yellow | n2 = Green | n3 = Red, for 20nm system with nD=4d24 and E0=1d8.

The oscillatory behavior that was observed was small, and will be discussed in the following section. The "change in state that is depicted corresponds to the accumulation of numerical error that mimics spontaneous emission.

3) Average Dynamic Behavior

After determining that there were unexpected dynamics in the system, some way of visualizing it had to be determined. Ideally, all 8 million time steps, $n = 8,000,000$, could be saved and analyzed. The problem with that, with double precision numbers and the grid size used, each simulation would generate $> 6\ TB$ of data. To avoid this, at each time step, the average of the energy state population was taken and recorded, resulting in only 1 GB

of data. It remains to be determined if there is a significant loss of important information but this analysis did provide some insights.
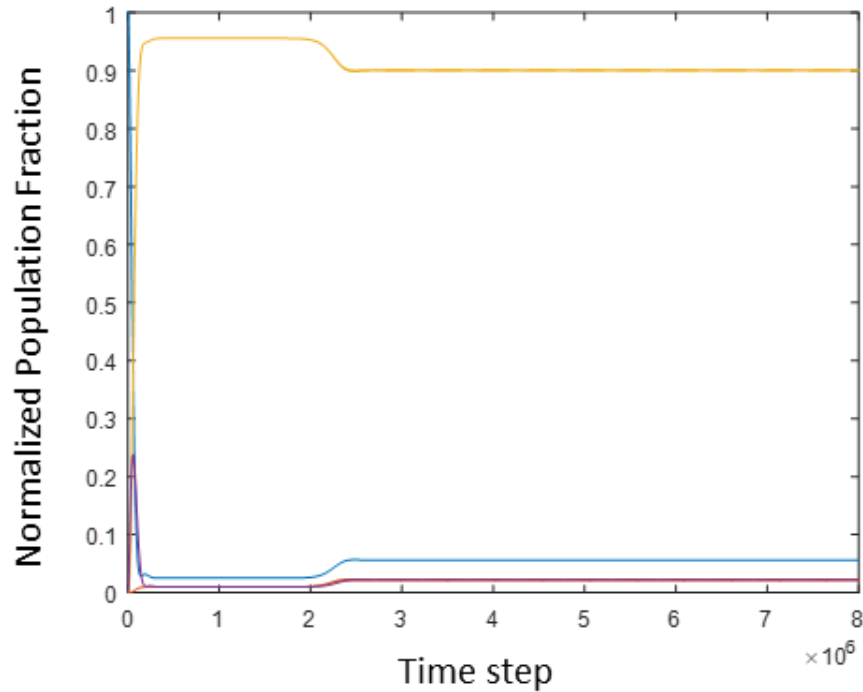
Figure 30: Average population of each level as a function of the time step, n0 = Blue | n1 = Orange (not visible) | n2 = Yellow | n3 = Red. Mt=20nm, nD=4d24, E0=1d8.

Figure 30 shows the results of this analysis for the $20 \ nm$ system with a molecular density of $4 \times 10^{24} \ \frac{molecules}{m^3}$ with a total of 8 million time steps for a total of $20 \ ps$, and $E0 = 1d8$, well within the lasing region. First, population inversion is clear. Second, the reader is asked to note the appearance of four different segments, one which exists from $0 < n < \sim 250{,}000$ in which the largest and most violent changes in population occur, including population inversion, the 1st "flat" segment from $\sim 250{,}000 < n < 2{,}000{,}000$, in which the population seems to be constant, another transient segment $2{,}000{,}000 < n <$

39

~2,333,000, and finally the 2nd flat segment from ~$2,333,000 < n < 8,000,000$. Zooming in on n1 population in the 4th region discussed, oscillations are present:
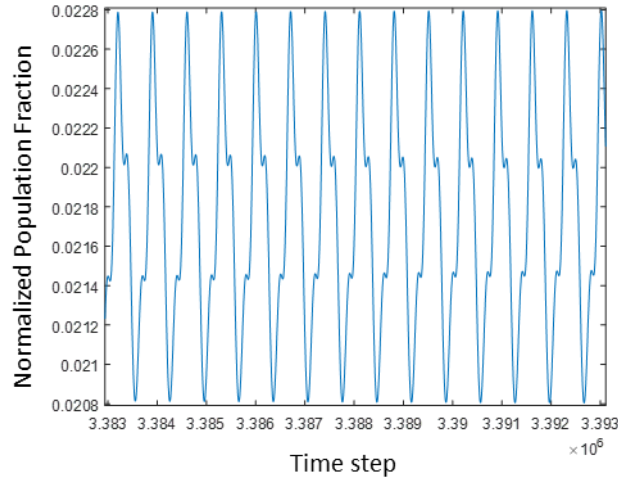
Figure 31: Zoomed in detail of n1 population dynamics in the 4th region

The oscillations are not large in amplitude which are ascribed to numerical artifacts. The "nudge" in the population during the second transient region shows the accumulation of the numerical errors which allow the system to finally lase, essentially, the errors built up enough to simulate the spontaneous emission of a photon which starts the cascade effect of lasing.

III. MOLECULAR ELECTRONICS

The theory of the molecules as used in Section II, is a manifestation of the Mean-filed approximation. To simulate molecules within a dynamic system, in addition to the electric properties, the quantum mechanical behavior must be modeled. The full mathematical treatment of quantum mechanics, however, can prove to be intractable, especially when

simulating many molecules within a greater system, since the full quantum solution would require every molecule to be entangled to the other in some way through the Hamiltonian of the system. A common approach to ease computation burden is to use the mean-field approximation in a simulation. In essence, the mean-field approximation decouples the dynamics of the molecules from each other directly and allows each to behave in a field generated by all of the others. Although, this approximation has been used extensively, generating experimentally verified results, and is perhaps the only way in which certain simulations can be accomplished, a more intimate knowledge the mean-field approximation would allow researchers to more finely tune simulations and to have a more complete picture of any subtleties that are perhaps hidden when using the approximation. The following preliminary work is an effort in the afore mentioned goals by comparing exact quantum formulations (EQFs) and the mean-field approximation (MFA) through Hamiltonian formalism. This part of the work is dedicated to laying the theoretical ground work for this endeavor and demonstrating preliminary findings. Work in this area is being actively pursued.

A. The Initial System - Dipoles

Of course, to begin this study, the system of molecules used in the previous simulations is far too complicated. This section will "build from the ground up" so to speak.

1) Molecules

The system with which we are concerning ourselves consists of a 1-D strand of dipoles, with an initial distribution of excitons. A general visualization of this system is given below:
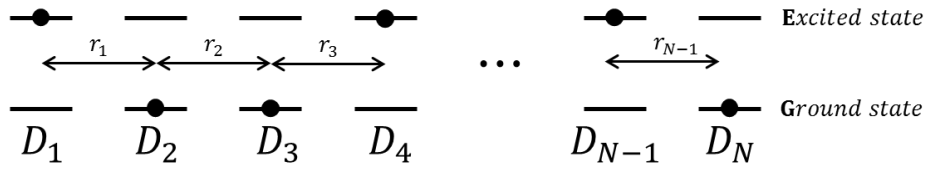
Figure 32: The General Model for a 1-D Strand of Molecules

This general model allows for N number of dipoles, any number of which is in the excited or ground states. The general model allows for the dipoles to each be a unique distance, r_i, apart and have a unique dipole moment, μ_i, as well. The degree of randomness in the number and locations of the excited states and the relative distances between dipoles is arbitrary.

However, to begin analysis of the system and conduct a comparison of the EQF and MFA, the general model is reduced to a more amenable one in which the dipoles are a fixed, identical distance, r, apart. Additionally, all dipoles have identical dipole moments, μ, and the system contains a singular exciton (dipole in the excited state) in the strand at any time, shown in Figure 33 below:

Figure 33: The Restricted Model for a 1-D Strad of Molecules with fixed, identical relative distances and a singular exciton present

An equivalent visualization of the above system is given below. Both schemes will be used, depending on the relative convenience of each scheme with respect to the scenario or methods under analysis:
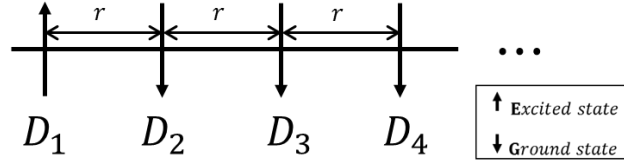
Figure 34: Equivalent Visualization with Arrows and orientation describing dipoles and states, respectively

2) The Potentials

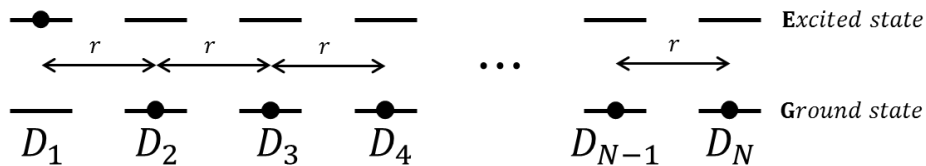Since the time dependent dipole distribution is sought, there will be dipole oscillations as the exciton moves from one dipole to another. To fully describe this, the electric field produced by an oscillating dipole is given below [13]:

$$\vec{E}(\vec{r}) = \frac{1}{4\pi\epsilon_0}\left\{\frac{\omega^2}{c^2 r}(\hat{r}\times\vec{\mu})\times\vec{r} + \left(\frac{1}{r^3} - \frac{i\omega}{cr^2}\right)[3\hat{r}(\hat{r}\cdot\vec{\mu}) - \vec{\mu}]\right\}e^{i\omega r/c} \qquad (3.1)$$
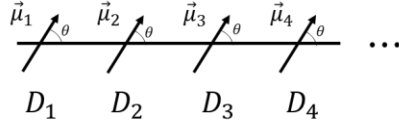
The dipole moment of the dipole producing the field is given by $\vec{\mu} = q\vec{d}$ and the wave vector is given by $k = \frac{\omega}{c}$. Now the system of dipoles is such that $r \ll k$, the electrostatic limit is approached and the only relevant part of the field produced by the dipole is given by the electrostatic expression:
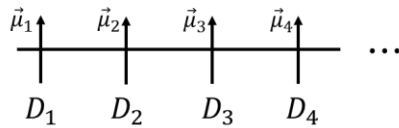
$$\vec{E}(\vec{r}) = \frac{1}{4\pi\epsilon_0}\frac{3\hat{r}(\hat{r}\cdot\vec{\mu}) - \vec{\mu}}{r^3} \qquad (3.2)$$

3) Molecular Orientations

From the above equation, it is simple to surmise that the relative orientation of the dipoles is important. For the time being, only identically oriented dipoles will be

43

considered; however, even with this constraint, electric field for each dipole has several possibilities given below.
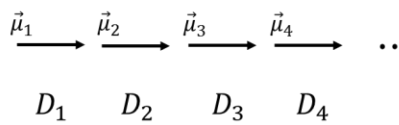
Figure 35: The General and Extrema Equations of the Electric field

In this work, the horizontal equation will be used, however, the methods can easily be extended to the general case, if working with a strand of dipoles in which all the dipoles are oriented the same was (a.k.a. θ is identical for all dipoles, even though the dipoles can be in the excited or ground state).

B. The Density Operator

The density operator of a system is generally defined as the following:

$$\rho = |\psi\rangle\langle\psi| \tag{3.3}$$

where ψ is the wave function of the system. Looking at the individual matrix elements of the density operator:

$$\rho = \sum_{j,j'} \rho_{j,j'} |j\rangle\langle j'| \tag{3.4}$$

44

In which the indices, j and j' correspond to the various states of the system. Density matrices are always square, with the diagonal elements $\rho_{j,j}$ interpreted as the probability of the system being in state j and the off diagonal terms $\rho_{j,j'}$ interpreted as coherences between states j and j'. To find the time dependence of the density operator:

$$\frac{\partial \rho}{\partial t} = \frac{\partial}{\partial t} |\psi\rangle\langle\psi| \tag{3.5}$$

$$\frac{\partial \rho}{\partial t} = |\psi\rangle\frac{\partial \langle\psi|}{\partial t} + \frac{\partial |\psi\rangle}{\partial t}\langle\psi| \tag{3.6}$$

Taking the time dependent Schrödinger equation and its complex conjugate:

$$\frac{\partial}{\partial t}|\psi\rangle = -\frac{i}{\hbar}H|\psi\rangle \ and \ \frac{\partial}{\partial t}\langle\psi| = \frac{i}{\hbar}\langle\psi|H \tag{3.7}$$

$$\frac{\partial \rho}{\partial t} = \frac{-i}{\hbar}(|\psi\rangle\langle\psi|H - H|\psi\rangle\langle\psi|) \tag{3.8}$$

$$\frac{\partial \rho}{\partial t} = -\frac{i}{\hbar}[H,\rho] \tag{3.9}$$

We arrive at the time dependence of the density operator. This is the fundamental working equation that will reveal the dynamics of an exciton in either the EQF or the MFA methods of evaluating the Hamiltonians and density matrices.

C. The Exact Quantum Formulation

The Exact Quantum Formulation refers the formalism that will be developed in the following section. The motivation of the name comes from the fact that this method considers the strand of dipoles as a singular system with multiple states, and does not assume any clever superposition or product of individual dipole states or systems to specify

45

the system. For the initial treatment and development of this work, a system of only three

dipoles will be considered.

1) The system and ρ

In the density matrix formulation, the general states of the system are considered, as

shown below for a three-dipole system with one exciton:
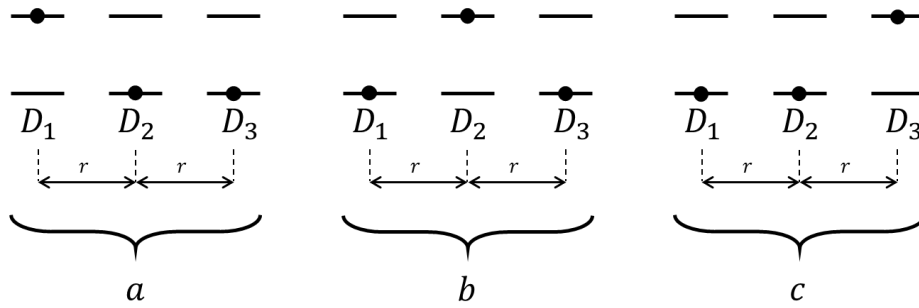
Figure 36: EQF Demarcation of States for a Three-dipole System with One Exciton

For a system with on exciton, there are N states equal to the number of dipoles. Recalling

the definition of ρ, in matrix form for this three-state system, would result in a 3×3 matrix.

At initial time $t = 0$, the exciton would be at one of the dipoles corresponding to one of

the above states, resulting in the following initial matrix:

$$\begin{pmatrix} \rho_{aa} & 0 & 0 \\ 0 & \rho_{bb} & 0 \\ 0 & 0 & \rho_{cc} \end{pmatrix} \tag{3.10}$$

where one of the diagonals is equal to 1, corresponding to a probability of 100% of the

exciton "existing at that dipole" or "in that state" (whichever one prefers), and the other

diagonals equal zero. Under the influence of the Hamiltonian, the density matric will evolve with time per equation 3. 9.

2) The Hamiltonian

To determine the time dependence of the density matrix, the Hamiltonian is needed. The Hamiltonian consists of the following parts, written in density operator form:

$$H_e = \sum_j E_j |j\rangle\langle j| \tag{3.11}$$

$$V = \sum_{j \neq j'} V_{j,j'} |j\rangle\langle j'| \tag{3.12}$$

where the states j and j' correspond to states a, b, and c. H_e represents the energy of the exciton in system. Under the present restrictions, the exciton exists with energy $E_j = E$ for all j. In matrix form, this corresponds to the diagonals being populated with the exciton energy. V represents the coupling between states. The states are coupled by the potential the dipoles exert on their neighbors, allowing the exciton to move between neighbors. In the definition above, the coupling only happens between different states, but could be achieved by defining all $V_{j,j} = 0$ and summing over all combinations. The $V_{j,j'}$ matrix elements are the potential between states j and j'. In the vertical orientation discussed above:

$$V_{j,j} = \sum_{j'} \mu_j \frac{\mu_{j'}}{r_{j,j'}^3} \tag{3.13}$$

Because we are considering only one exciton, the dipole which has the exciton will always be in the opposite orientation of the other dipoles, which is why the term is positive. In the nearest neighbor approximation, only state b consists of a sum of terms as it can couple to

47

both states a or b, while a and c cannot directly couple to each other. The Hamiltonian is given as the following:

$$H = H_e + V \qquad (3.14)$$

For the nearest neighbor approximation in the three-state system with identical distances r and identical dipole moments μ, the Hamiltonian will take the following matrix form:

$$\begin{pmatrix} E & \mu^2/r^3 & 0 \\ \mu^2/r^3 & E & \mu^2/r^3 \\ 0 & \mu^2/r^3 & E \end{pmatrix} \qquad (3.15)$$

D. The Mean Field Approximation

The Mean Field Approximation refers the formalism developed in the following section. As will be shown, the name derives from the final form of the approximation which decouples all the dipoles from each other, each one acting through the collective influence of the others through a "mean field."

1) The system and ρ

The mean field approximation seeks to simplify the resulting equations given by the DFA. To do this, the system is considered to be a product of the individual density matrices of the individual dipoles instead of an explicit entity. The system is shown as follows:
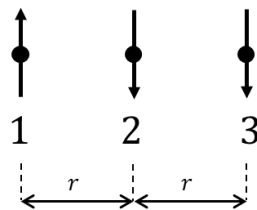

Figure 37: MFA System as a product of 3, two state systems

48

For the above picture, which is one of the three possible ways that this product system can be, the density matrix is given as the following:

$$\rho = \otimes_j \rho_j \qquad (3.16)$$

$$\rho = \begin{pmatrix} 1 & 0 \\ 0 & 0 \end{pmatrix} \otimes \begin{pmatrix} 0 & 0 \\ 0 & 1 \end{pmatrix} \otimes \begin{pmatrix} 0 & 0 \\ 0 & 1 \end{pmatrix} \qquad (3.17)$$

Where ρ_{11} is the excited state for a dipole and ρ_{22} is the ground state, and j is the dipole index, not the state index as in the EQF.

2) The Hamiltonian

Because of the density matrix being formulated as above, this approximation allows for a simplification of the final dynamical equations, only after some more complicated manipulations however. The Hamiltonian for the system itself is a bit more complicated and is given as follows:

$$H = \sum_j H_j^{(1)} + \sum_{j \neq j'} H_{jj'}^{(2)} \qquad (3.18)$$

The operators $H_j^{(1)}$ correspond to the single body Hamiltonians that act only on the dipole j and delineate the energy of the excited state and the ground state, for example:

$$H_j^{(1)} = \begin{pmatrix} E & 0 \\ 0 & 0 \end{pmatrix} \qquad (3.19)$$

And are all identical as the dipoles are identical, however, it is important to emphasize that each $H_j^{(1)}$ only operates on the dipole j. The operators $H_{jj'}^{(2)}$ are the coupling operators which serve to connect the individual dipoles together though potentials. Again, each $H_{jj'}^{(2)}$

49

will only act upon states j and j' at a time. As an example, since dipole 2 can couple with both 1 and 3 in the nearest neighbor approximation:

$$H_{21}^{(2)} = \begin{pmatrix} 0 & 0 \\ \mu^2/r^3 & 0 \end{pmatrix} \tag{3.20}$$

$$H_{23}^{(2)} = \begin{pmatrix} 0 & \mu^2/r^3 \\ 0 & 0 \end{pmatrix} \tag{3.21}$$

Again, these matrices were generated under the assumption that the dipole moments and inter-dipole distances are identical. Now, the power of the mean field approximation is apparent in the derivation that follows. Taking the time dependent equation of the density operator and substituting equation (3.16):

$$\frac{\partial \rho}{\partial t} = -\frac{i}{\hbar}[H, \rho] \tag{3.22}$$

$$\frac{\partial}{\partial t}\left(\otimes_j \rho_j\right) = -\frac{i}{\hbar}\left[H, \left(\otimes_j \rho_j\right)\right] \tag{3.23}$$

$$\frac{\partial}{\partial t}\left(\otimes_j \rho_j\right) = -\frac{i}{\hbar}\left(H \otimes_j \rho_j - \otimes_j \rho_j H\right) \tag{3.24}$$

The terms of the commutator can be expanded as follows, recalling that the indexed Hamiltonians only act on the corresponding indexed density matrices:

$$H\left(\otimes_j \rho_j\right) = \sum_j H_j^{(1)}\left(\otimes_j \rho_j\right) + \sum_{j \neq j'} H_{jj'}^{(2)}\left(\otimes_j \rho_j\right)$$

$$= \sum_j \left(\otimes_{k \neq j} \rho_k\right) \otimes H_j^{(1)} \rho_j + \sum_{j \neq j'}\left(\otimes_{k \neq j,j'} \rho_k\right) \otimes H_{jj'}^{(2)} \rho_j \rho_{j'} \tag{3.25}$$

And:

$$\left(\otimes_j \rho_j\right)H = \sum_j \left(\otimes_j \rho_j\right)H_j^{(1)} + \sum_{j \neq j'}\left(\otimes_j \rho_j\right)H_{jj'}^{(2)}$$

$$= \sum_j \left(\otimes_{k \neq j} \rho_k \right) \otimes \rho_j H_j^{(1)} + \sum_{j \neq j'} \left(\otimes_{k \neq j,j'} \rho_k \right) \otimes \rho_j \rho_{j'} H_{jj'}^{(2)} \quad (3.26)$$

At this point, the MFA seems to be far more trouble than its worth, with rather large matrices as the result of the tensor products. However, if the trace is taken of all states except for state $j = a$, a very useful result is obtained. Recalling that the trace of a density matrix of a pure state is 1 and some other useful identities (where A and B are matrices and c is a scalar):

$$\mathrm{Tr}(\rho) = 1 \quad (3.27)$$

$$\mathrm{Tr}(A + B) = \mathrm{Tr}(A) + \mathrm{Tr}(B) \quad (3.28)$$

$$\mathrm{Tr}(AB) = \mathrm{Tr}(BA) \quad (3.29)$$

$$\mathrm{Tr}(cB) = c\,\mathrm{Tr}(A) \quad (3.30)$$

$$\mathrm{Tr}(A \otimes B) = \mathrm{Tr}(A)\,\mathrm{Tr}(B) \quad (3.31)$$

$$\mathrm{Tr}(\rho H) = \langle H \rangle \quad (3.32)$$

The last of which is that the trace of an operator and the density matrix is the expectation value of the operator. The trace over all dipoles except dipole $j = a$ is taken:

$$\mathrm{Tr}_{j \neq a} \left(\frac{\partial}{\partial t} \left(\otimes_j \rho_j \right) \right) = -\frac{i}{\hbar} \left(H \otimes_j \rho_j - \otimes_j \rho_j H \right) \quad (3.33)$$

Recalling the identity in equation (3.31):

$$\frac{\partial}{\partial t} \left(\prod_{j \neq a} \mathrm{Tr}(\rho_j) \times \rho_a \right) = \mathrm{Tr}_{j \neq a} \left(-\frac{i}{\hbar} \left(H \otimes_j \rho_j - \otimes_j \rho_j H \right) \right) \quad (3.34)$$

And as the trace of a density matrix is unity:

$$\frac{\partial \rho_a}{\partial t} = -\frac{i}{\hbar}\left(\mathrm{Tr}_{j\neq a}(H \otimes_j \rho_j) - \mathrm{Tr}_{j\neq a}(\otimes_j \rho_j H)\right) \qquad (3.35)$$

Already, an interesting simplification in that we can look at the time dependence of a single dipole's density matrix. Now, let's look at just the first term of the commutator in (3. 35)

$$\mathrm{Tr}_{j\neq a}\left(H(\otimes_j \rho_j)\right)$$

$$= \mathrm{Tr}_{j\neq a}\left(\sum_j (\otimes_{k\neq j} \rho_k) \otimes H_j^{(1)} \rho_j + \sum_{j\neq j'} (\otimes_{k\neq j,j'} \rho_k) \otimes H_{jj'}^{(2)} \rho_j \rho_{j'}\right)$$

Using Equation 3. 28:

$$= \sum_j \mathrm{Tr}_{j\neq a}(\otimes_{k\neq j} \rho_k) \times \mathrm{Tr}_{j\neq a}\left(H_j^{(1)}\rho_j\right) + \sum_{j\neq j'} \mathrm{Tr}_{j\neq a}(\otimes_{k\neq j,j'} \rho_k) \times \mathrm{Tr}_{j\neq a}\left(H_{jj'}^{(2)}\rho_j\rho_{j'}\right)$$

Followed by Equation 3. 31:

$$= \sum_j \prod_{k\neq j} \mathrm{Tr}_{j\neq a}(\rho_k) \times \mathrm{Tr}_{j\neq a}\left(H_j^{(1)}\rho_j\right) + \sum_{j\neq j'} \prod_{k\neq j,j'} \mathrm{Tr}_{j\neq a}(\rho_k) \times \mathrm{Tr}_{j\neq a}\left(H_{jj'}^{(2)}\rho_j\rho_{j'}\right)$$

And due to Equation 3. 27:

$$= \sum_j \mathrm{Tr}_{j\neq a}\left(H_j^{(1)}\rho_j\right) + \sum_{j\neq j'} \mathrm{Tr}_{j\neq a}\left(H_{jj'}^{(2)}\rho_j\rho_{j'}\right) \qquad (3.36)$$

Now expanding the sums:

$$= H_a^{(1)}\rho_a + \sum_{j\neq a}\mathrm{Tr}\left(H_j^{(1)}\rho_j\right) + \sum_{j=a,j'}\mathrm{Tr}\left(H_{aj'}^{(2)}\rho_{j'}\right)\rho_a + \sum_{j,j'=a}\mathrm{Tr}\left(H_{ja}^{(2)}\rho_j\right)\rho_a$$

$$+ \sum_{j\neq j'\neq a}\mathrm{Tr}\left(H_{jj'}^{(2)}\rho_j\rho_{j'}\right)$$

Which can be rewritten using equation 3. 32:

$$= H_a^{(1)} \rho_a + \sum_{j \neq a} \text{Tr}\left(H_j^{(1)} \rho_j\right) + \sum_{j=a,j'} \langle H_{aj'}^{(2)} \rangle_{j'} \rho_a + \sum_{j,j'=a} \langle H_{ja}^{(2)} \rangle_j \rho_a +$$

$$\sum_{j \neq j' \neq a} \text{Tr}\left(H_{jj'}^{(2)} \rho_j \rho_{j'}\right) \tag{3.37}$$

Where $\langle H_{ja}^{(2)} \rangle$ is taken to mean the expectation value of the coupling term between state a and state j. The subscript j within the sums serves to indicate the sum over all $j \neq a$. And similarly, for the second term in (3.35):

$$\text{Tr}_{j \neq a}\left((\otimes_j \rho_j)H\right) = \text{Tr}_{j \neq a}\left(\sum_j (\otimes_{k \neq j} \rho_k) \otimes \rho_j H_j^{(1)} + \sum_{j \neq j'} (\otimes_{k \neq j,j'} \rho_k) \otimes \rho_j \rho_{j'} H_{jj'}^{(2)}\right)$$

Using Equation 3.28:

$$= \sum_j \text{Tr}_{j \neq a}(\otimes_{k \neq j} \rho_k) \times \text{Tr}_{j \neq a}\left(\rho_j H_j^{(1)}\right) + \sum_{j \neq j'} \text{Tr}_{j \neq a}(\otimes_{k \neq j,j'} \rho_k) \times \text{Tr}_{j \neq a}\left(\rho_j \rho_{j'} H_{jj'}^{(2)}\right)$$

Followed by Equation 3.31 and 3.27:

$$= \sum_j \prod_{k \neq j} \text{Tr}_{j \neq a}(\rho_k) \times \text{Tr}_{j \neq a}\left(\rho_j H_j^{(1)}\right) + \sum_{j \neq j'} \prod_{k \neq j,j'} \text{Tr}_{j \neq a}(\rho_k) \times \text{Tr}_{j \neq a}\left(\rho_j \rho_{j'} H_{jj'}^{(2)}\right)$$

$$= \sum_j \text{Tr}_{j \neq a}\left(\rho_j H_j^{(1)}\right) + \sum_{j \neq j'} \text{Tr}_{j \neq a}\left(\rho_j \rho_{j'} H_{jj'}^{(2)}\right) \tag{3.38}$$

Now expanding the sums:

$$= \rho_a H_a^{(1)} + \sum_{j \neq a} \text{Tr}\left(\rho_j H_j^{(1)}\right) + \sum_{j=a,j'} \rho_a \text{Tr}\left(\rho_{j'} H_{aj'}^{(2)}\right) + \sum_{j,j'=a} \rho_a \text{Tr}\left(\rho_j H_{ja}^{(2)}\right)$$

$$+ \sum_{j \neq j' \neq a} \text{Tr}\left(\rho_j \rho_{j'} H_{jj'}^{(2)}\right)$$

Which can be rewritten using equation 3.32:

$$= \rho_a H_a^{(1)} + \sum_{j \neq a} \text{Tr}\left(\rho_j H_j^{(1)}\right) + \sum_{j=a,j'} \rho_a \langle H_{aj'}^{(2)} \rangle_{j'} + \sum_{j,j'=a} \rho_a \langle H_{ja}^{(2)} \rangle_j +$$

$$\sum_{j \neq j' \neq a} \text{Tr}\left(\rho_j \rho_{j'} H_{jj'}^{(2)}\right) \tag{3.39}$$

Now, taking the difference of Equations 3.37 and 3.39 to evaluate Equation 3.35:

$$\left(H_a^{(1)} \rho_a + \sum_{j \neq a} \text{Tr}\left(H_j^{(1)} \rho_j\right) + \sum_{j=a,j'} \langle H_{aj'}^{(2)} \rangle_{j'} \rho_a + \sum_{j,j'=a} \langle H_{ja}^{(2)} \rangle_j \rho_a \right.$$

$$\left. + \sum_{j \neq j' \neq a} \text{Tr}\left(H_{jj'}^{(2)} \rho_j \rho_{j'}\right) \right)$$

$$- \left(\rho_a H_a^{(1)} + \sum_{j \neq a} \text{Tr}\left(\rho_j H_j^{(1)}\right) + \sum_{j=a,j'} \rho_a \langle H_{aj'}^{(2)} \rangle_{j'} + \sum_{j,j'=a} \rho_a \langle H_{ja}^{(2)} \rangle_j \right.$$

$$\left. + \sum_{j \neq j' \neq a} \text{Tr}\left(\rho_j \rho_{j'} H_{jj'}^{(2)}\right) \right) = \text{Tr}_{j \neq a}\left(H \otimes_j \rho_j\right) - \text{Tr}_{j \neq a}\left(\otimes_j \rho_j H\right)$$

The second and third terms of each of the commutator terms are the same, and subtract out:

$$= H_a^{(1)} \rho_a + \sum_{j=a,j'} \langle H_{aj'}^{(2)} \rangle_{j'} \rho_a + \sum_{j,j'=a} \langle H_{ja}^{(2)} \rangle_j \rho_a - \rho_a H_a^{(1)} - \sum_{j=a,j'} \rho_a \langle H_{aj'}^{(2)} \rangle_{j'}$$

$$- \sum_{j,j'=a} \rho_a \langle H_{ja}^{(2)} \rangle_j$$

And rewriting in terms of commutators:

$$\text{Tr}_{j \neq a}\left(H \otimes_j \rho_j\right) - \text{Tr}_{j \neq a}\left(\otimes_j \rho_j H\right) = \left[H_a^{(1)}, \rho_a\right] + \sum_{j'} \left[\langle H_{aj'}^{(2)} \rangle_{j'}, \rho_a\right] + \sum_j \left[\langle H_{ja}^{(2)} \rangle_j, \rho_a\right]$$

$$= \left[\left(H_a^{(1)} + \sum_{j'} \langle H_{aj'}^{(2)} \rangle_{j'} + \sum_j \langle H_{ja}^{(2)} \rangle_j\right), \rho_a\right] \tag{3.40}$$

Now, considering these terms as matrices, and considering the j index to be the row index and j' to be the column index, the first sum sums the column portions of the coupling terms and the second sum sums the row portions of the coupling terms. Putting these together, the final expression, which is also quite intuitive is as follows:

$$\frac{\partial \rho_a}{\partial t} = -\frac{i}{\hbar}\left[\left(H_a^{(1)} + \Sigma_j\langle V\rangle_{j\to a}\right), \rho_a\right] \tag{3.41}$$

This final equation reads: The time-rate of change in the density matrix of dipole a is proportional to the commutator of single-body Hamiltonian of dipole a plus the potential (coupling) felt by dipole a from all other dipoles j. In other words, each dipole will react based its energy and the potential of all the other dipoles to which it is coupled.

To emphasize, the formulation of the mean-field approximation as derived above uses Hamiltonian formalism. In practice, especially when the potential is a function of electric fields, the Hamiltonian formalism may not be explicitly used but the idea is equivalent. Equations 1.15 are mean-field equations, but however were not developed with Hamiltonian formalism since they are semi-classical, not quantum based.

E. Preliminary Results

   1) A brief description of the code

The development of a robust code that could generate preliminary results was an enlightening, yet difficult process. In the first iteration, the nine differential equations necessary for the EQF of a system of three dipoles under nearest neighbor approximation were determined by defining a commutation relationship, and letting Mathematica do the algebra. Then, by hand, the 4$^{\text{th}}$ order Runge-Kutta procedure was implemented. Needless

to say, this was problematic because every system with a different number of dipoles, N, would have a different number of differential equations. The way in which the Hamiltonian was defined was similarly lacking in robustness. When the MFA of a system of 3 dipoles was attempted the first time, the 12 resulting equations made it necessary to develop a way more advanced than implementation by hand. About 60 iterations later, a robust script that will generate the Runge-Kutta for system of N dipoles (with reasonable neighbor approximations in the potential) and equal dipole moments was developed. The user need only specify a few parameters. The results from this code will be presented in the following.

Although the code works and generates results, it is inefficient and does not run quickly on personal computers. As will be mentioned in Section IV, the translation of the code to a MPI capable system will be pursued.

All the results that follow share the following restrictions: 1) for the two-body Hamiltonians (the potential terms), the nearest neighbor condition is enforced, 2) all the dipole moments have identical magnitudes, and 3) the exciton energy at every dipole is identical as well.

The variations will be stated and include the number of dipoles and the time step size, h. Included with each result are the expectation value of the Hamiltonian, $E = \langle H \rangle = \text{Tr}(\rho H)$ at each time step and the $\text{Tr}(\rho)$ to verify whether the energy of the system is conserved and the density is conserved, respectively. The standard variable values are $E = 2$, $\mu = 1$, and $\hbar = 1$, in atomic units.

2) Coherence-less Initial Conditions in EQF

The coherence-less initial conditions result in an initial density matrix with elements $\rho_{11} = E$ and $\rho_{ij \neq 1} = 0$. The first system observed was a simple 2-dipole system. The probability density of the dipoles oscillates consistently between 0 and 1 as shown in Figure 38. The energy of the system is indeed conserved as demonstrated in Figure 39. Finally, in Figure 40, the trace of the density matrix is consistently at unity for the simulation. Unless there is deviation, the energy and density trace plots will not be demonstrated.
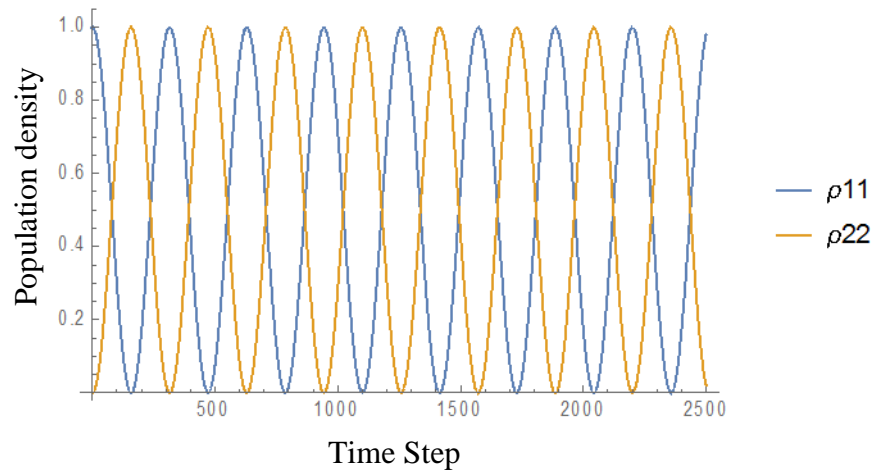
Figure 38: EQF population density result of a 2-dipole system with elements $\rho_{11} = E$ and $\rho_{ij \neq 1} = 0$ initial condition.
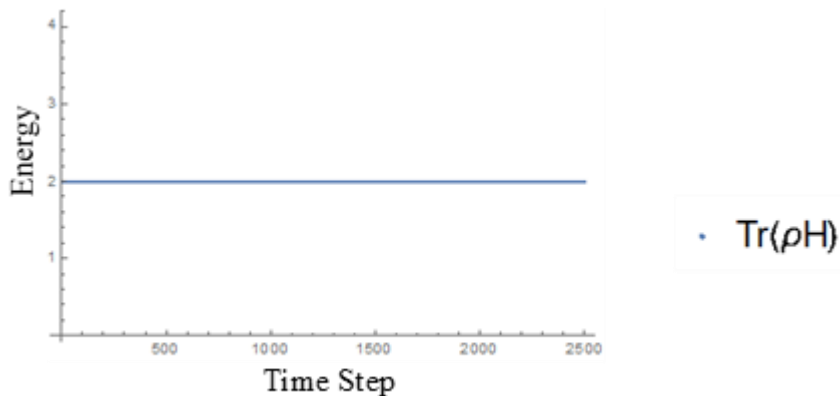
Figure 39: EQF energy result of a 2-dipole system with elements $\rho_{11} = E$ and $\rho_{ij \neq 1} = 0$ initial condition.
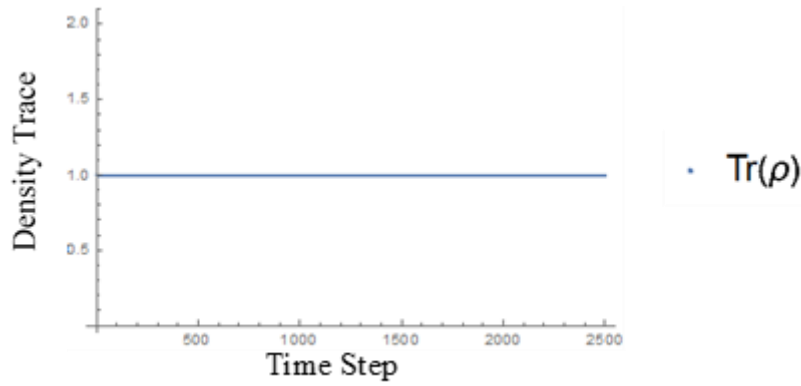
Figure 40: EQF density result of a 2-dipole system with elements $\rho_{11} = E$ and $\rho_{ij \neq 1} = 0$ initial condition.

With 3-dipoles, shown in Figure 41, the exciton's probability of being at any dipole oscillates consistently, although the chance that the exciton finds itself at the center dipole is half that of the others. The energy and the density are conserved, as before.
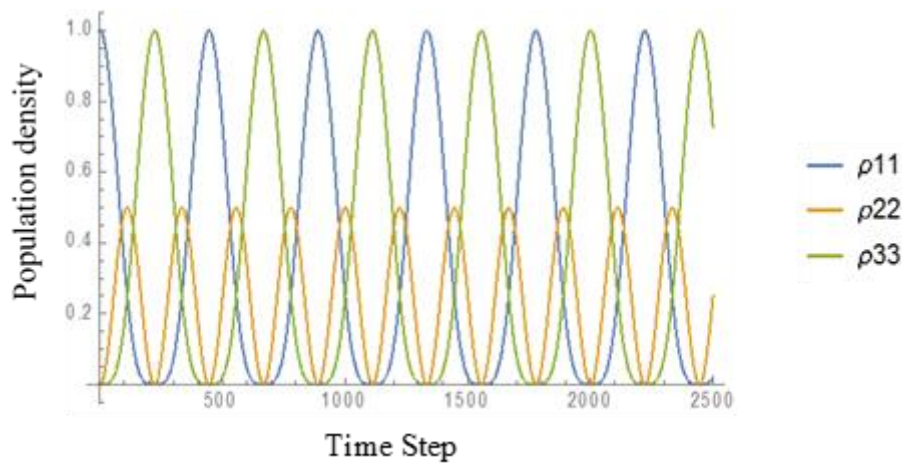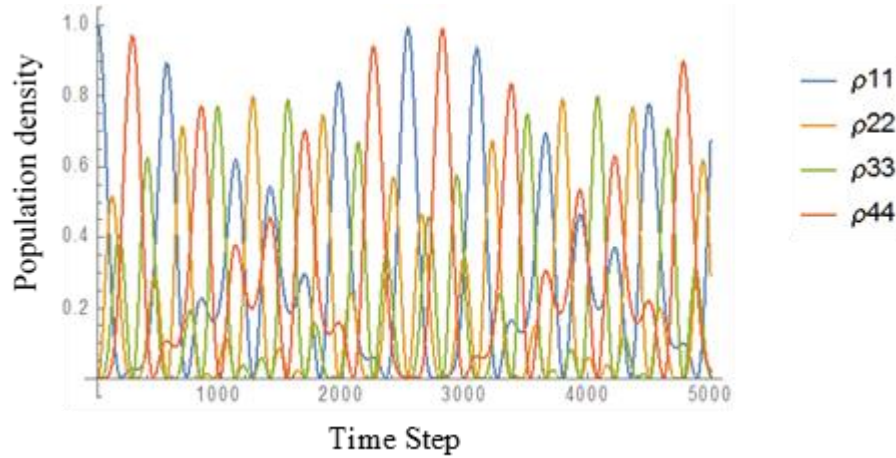

Figure 41: EQF population density result of a 3-dipole system with elements $\rho_{11} = E$ and $\rho_{ij \neq 1} = 0$ initial condition.

With 4-dipoles, the exciton's probability of being at any dipole has a more complicated oscillation for each dipole. The energy and the density are conserved. The simulations for

58

5 and 6 dipoles are not included here but increase in complexity, respectively, but the energy and density are conserved.

Figure 42: EQF population density result of a 4-dipole system with elements $\rho_{11} = E$ and $\rho_{ij \neq 1} = 0$ initial condition.

3) Coherence-less Initial Conditions in MFA

The simulation for the MFA was run with varying numbers of dipoles, but, the results were the same as in Figure 43 for two dipoles– no dynamics.
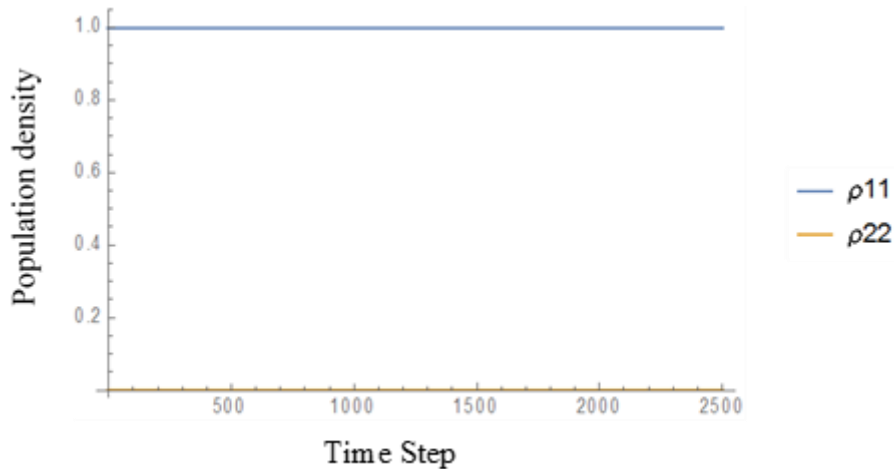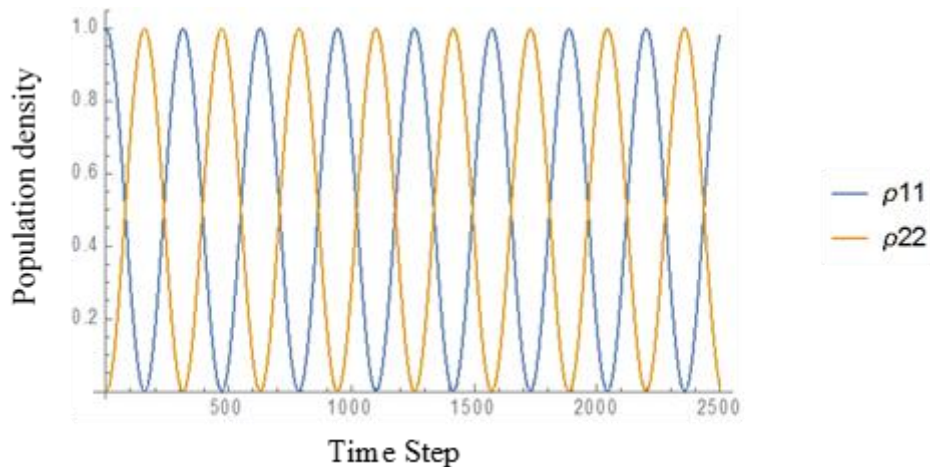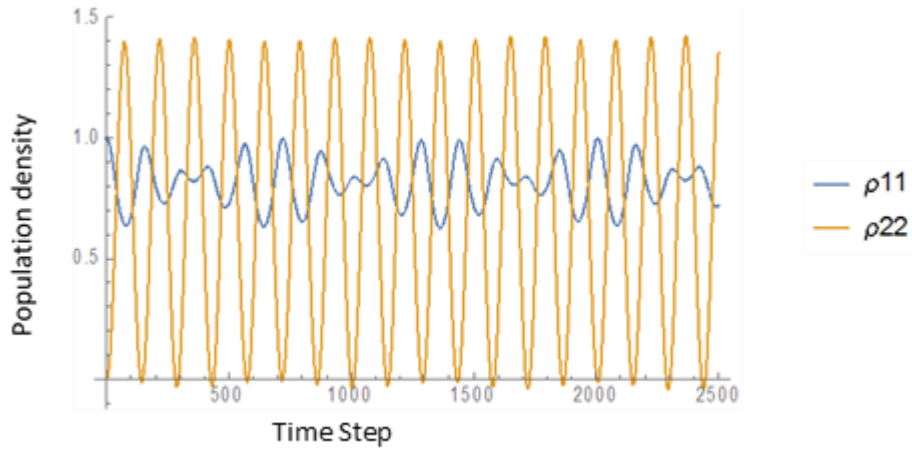

Figure 43: MFA population density result of a 2-dipole system with elements $\rho_{11} = E$ and $\rho_{ij \neq 1} = 0$ initial condition.

59

The first comparative result: EQF gives dynamics while the MFA does not. This holds true for any number of dipoles in the MFA: the exciton stays at its initial dipole and has no dynamics. This can be shown mathematically theoretically. Since ρ_a is a 2×2 matrix with off-diagonal zeros, and the 2-body Hamiltonian for each ρ_j is a 2×2 matrix with on off-diagonal terms:

$$\rho_a V = \begin{pmatrix} \rho_{11} & 0 \\ 0 & \rho_{22} \end{pmatrix} \begin{pmatrix} 0 & V_{j \to a} \\ V_{j \to a} & 0 \end{pmatrix} = V_{j \to a} \begin{pmatrix} 0 & \rho_{11} \\ \rho_{22} & 0 \end{pmatrix} \tag{3.42}$$

Which will always lead to a trace of zero:

$$\mathrm{Tr}(\rho_a V) = 0 \tag{3.43}$$

Which leads to a dynamical equation of the following from:

$$\frac{\partial \rho_a}{\partial t} = -\frac{i}{\hbar} \left[H_a^{(1)}, \rho_a \right] = -\frac{i}{\hbar} \left(\begin{pmatrix} E & 0 \\ 0 & 0 \end{pmatrix} \begin{pmatrix} \rho_{11} & 0 \\ 0 & \rho_{22} \end{pmatrix} - \begin{pmatrix} \rho_{11} & 0 \\ 0 & \rho_{22} \end{pmatrix} \begin{pmatrix} E & 0 \\ 0 & 0 \end{pmatrix} \right)$$

$$= -\frac{i}{\hbar} \left(\begin{pmatrix} E\rho_{11} & 0 \\ 0 & 0 \end{pmatrix} - \begin{pmatrix} E\rho_{11} & 0 \\ 0 & 0 \end{pmatrix} \right) = 0 \tag{3.44}$$

Which demonstrates a limitation of the MFA. Only through an initial condition containing coherences (off-diagonal matrix terms in ρ) can the MFA deliver dynamics. The density and energy are, obviously conserved and this behavior was observed for all simulations conducted with the MFA under coherence-less initial conditions.

4) Coherence Initial Conditions EQF

The following results were started with the initial condition of the singular exciton starting at dipole 1 with coherences. The physicality of setting the off-diagonal elements to a number, arbitrarily, is hard to justify. These simulations are to be taken more as a proof

60

of concept. Also, not included in this section are some of the simulations done for 3-dipole systems with coherence since the placement of coherences in the EQF was very difficult to match for the MFA case and there was no good comparison. $E = 1$ for these tests. Unless otherwise noted, all parameters remain unchanged.

Adding a coherence of 1, did not alter the general appearance of the EQF 2-dipole system as observed in Figure 44. The energy was constant but at a value of 3 and the trace was unity throughout. Adding the coherence of 1 to the MFA did produce dynamics as shown in Figure 45. The population densities do oscillate, however, not in a similar way to the EQF and not in a physical way, as $\rho 11$ becomes greater than 1 and less than 0. The energy of the system has oscillations and a downward trend that, while small, is noticeable in Figure 46.

Figure 44: EQF population density result of a 2-dipole system with elements $\rho_{11} = E$, $\rho_{i \neq j} = 1$ and $\rho_{22} = 0$ initial condition.

Figure 45: MFA population density result of a 2-dipole system with elements $\rho_{11} = E$, $\rho_{i \neq j} = 1$ and $\rho_{22} = 0$ initial condition.
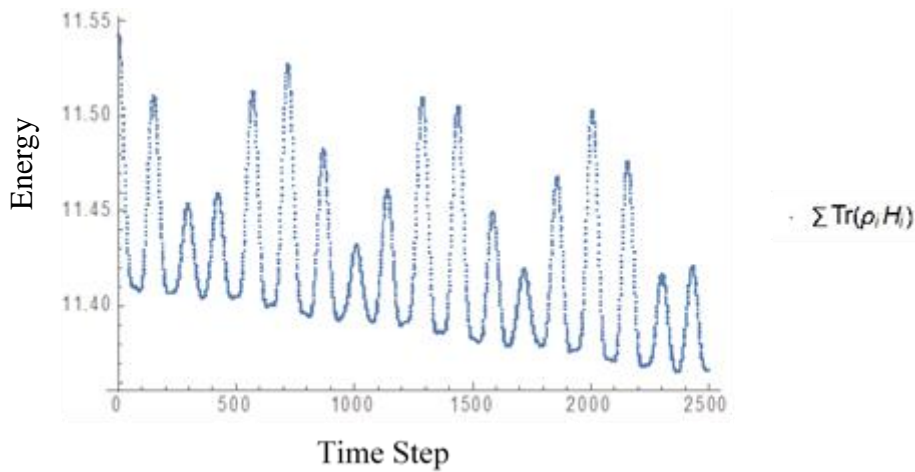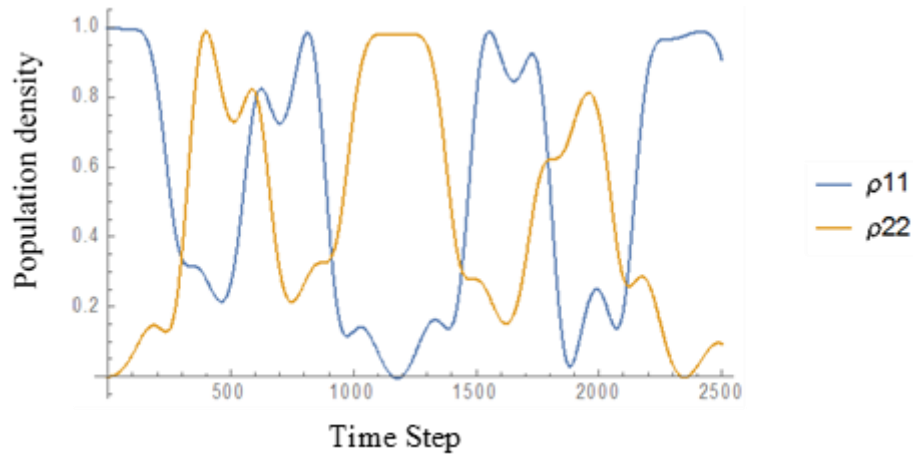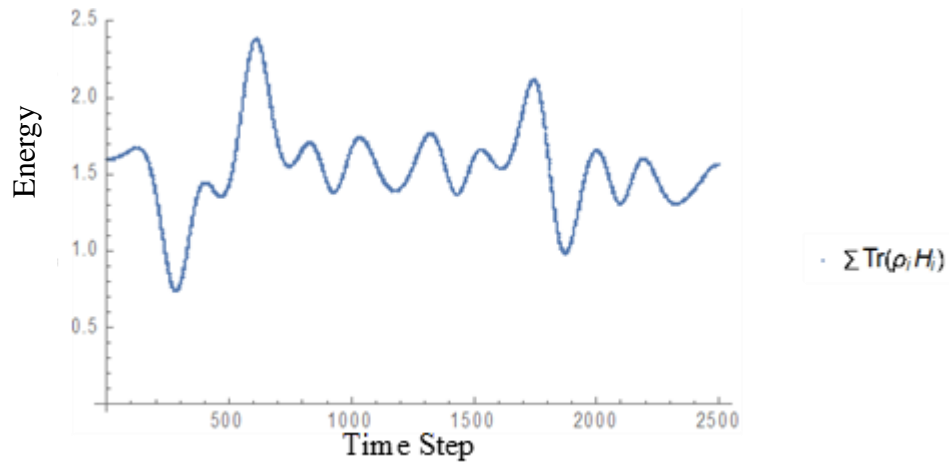

Figure 46: Energy of MFA in Figure 45

The coherence term was reduced to a value of 0.1 for both the EQF and MFA. The densities of the EQF had the exact same behavior as when the coherence was set to 1, The only difference being that the energy was conserved at a value of 1.2 instead of 3, and will not

be shown. The MFA however had a significant change, shown in Figure 47 and Figure 48. The oscillations are physical and the energy is far closer to the EQF value.

Figure 47: MFA population density result of a 2-dipole system with elements $\rho_{11} = E$, $\rho_{i \neq j} = 0.1$ and $\rho_{22} = 0$ initial condition.

Figure 48: Energy of MFA in Figure 47

5) Time step Testing

The time step importance was first noticed by accident, when the dipole moment was set to $\mu = 6$ instead of unity as in the previous tests. The time step interval was left as the original value of $h = 0.01$. Figure 49 shows the difference between the time step results. With a larger time step, the dipoles collapse to their average value, while with the smaller time step, the oscillations are sustained. The total number of time steps was adjusted for viewing ease. The energy is conserved at 77 and the density is covered at unity.
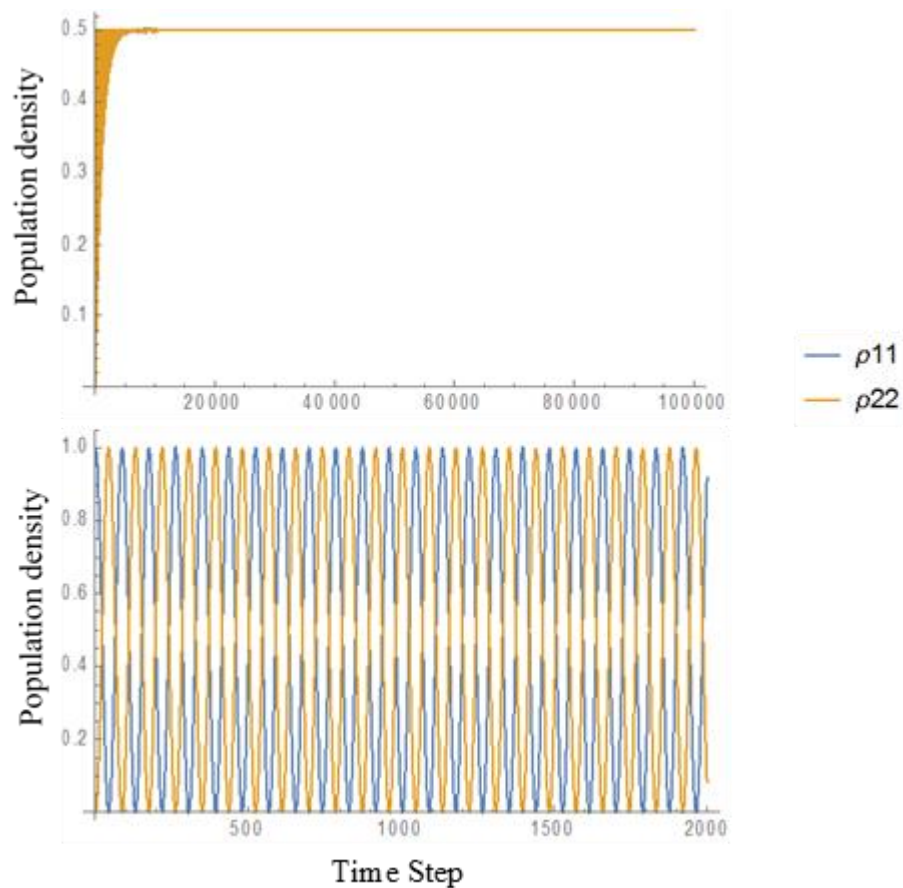
Figure 49: EQF population density results. Top: $h = 0.01$. Bottom: $h = 0.001$. Both with coherence term of unity and $\mu = 6$

Essentially the same behavior is noticed for the MFA. The larger time step cause the oscillations to collapse to their average values while the oscillations are sustained with a smaller time step, as noted in Figure 50.
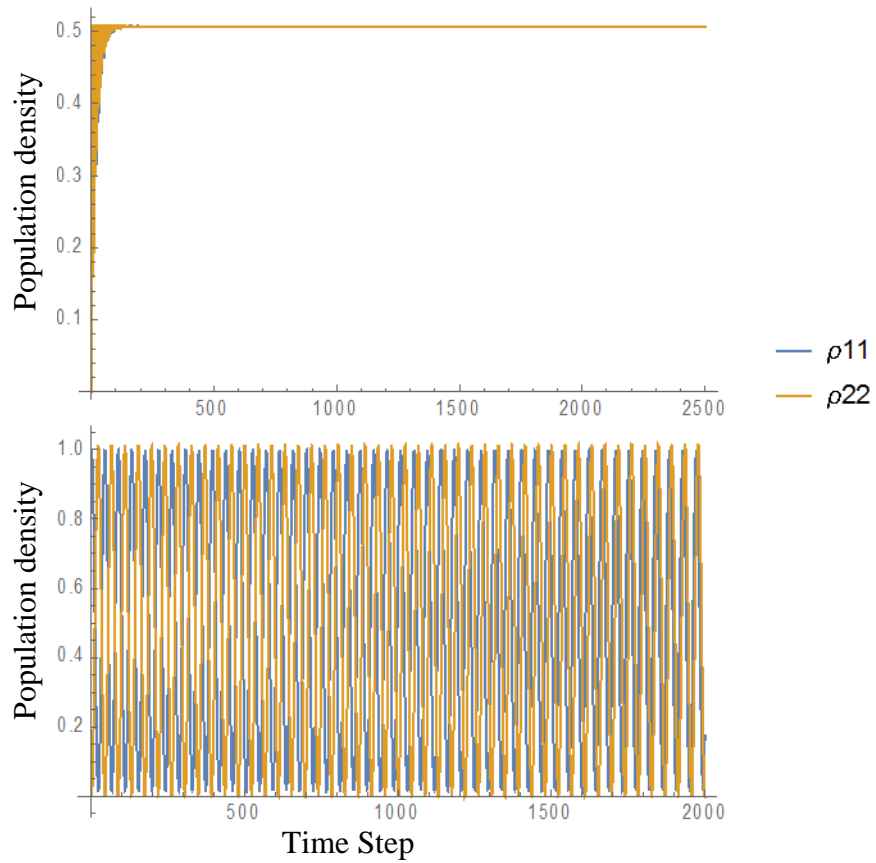

Figure 50: MFA population density results. Top: $h = 0.01$. Bottom: $h = 0.001$. Both with coherence term of unity and $\mu = 6$

The density is conserved for both scenarios, but the behavior of the energy is quite different as shown in Figure 51. The Energy is far off from the EQF value (most likely due to the

high coherence). Note that the energy falls to a value for the larger time step but stays right around that value for the smaller time step.
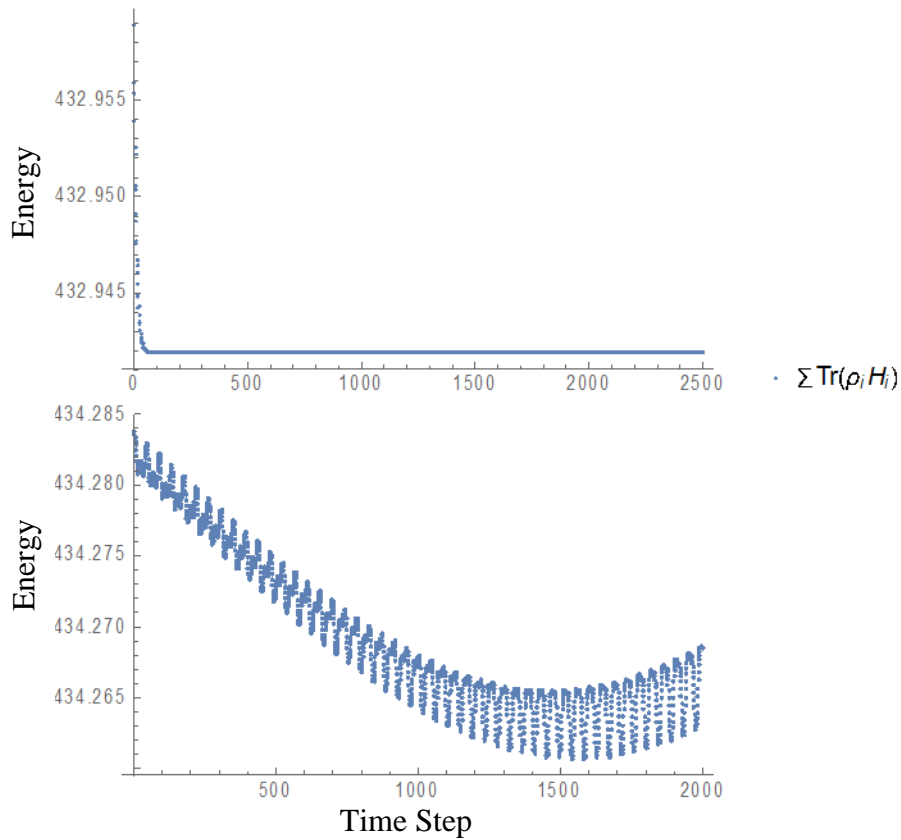
Figure 51: Energy results for Figure 50

The primary results that have been determined in this section are as follows:

1. The MFA cannot produce dynamics unless coherences are present.

2. The MFA rarely, perfectly conserves energy, but does approach the EQF when the coherences are small.

3. The time step which is used must be chosen carefully, as a large enough time step will cause the oscillation to collapse to their average.

IV. CONCLUSION

A. Reiteration of Findings

Several key insights and phenomenologies were developed and observed in this work. In Section II, the lasing profile was developed as a useful analysis graphic to view threshold and saturation phenomenology. The increase of the lasing region was observed as a function of molecular layer thickness and molecular density, and it was determined that the system can tolerate detuning only up to $\pm 2\%$.

The molecular population dynamics were observed to behave in exceeding interesting ways. There are two distinct flat segments that appear when a system will lase, showing the accumulation or error that causes the simulated, spontaneous emission. Outside of the lasing region, population inversion might occur, but there are no longer two flat segments, just one.

Finally, in Section III, the EQF and MFA were compared in a preliminary study. It was found that The MFA cannot produce dynamics unless coherences are present. The MFA rarely perfectly conserves energy, but does approach the EQF when the coherences are small. The time step which is used my be chosen carefully, as a large enough time step will cause the oscillation to collapse to their average.

B. Future Work

There are three major areas of research which will be pursed due to the findings of this work – Molecular Population Density dynamics analysis, System Identification Phenomenology, and Molecular Approximation Analysis. Each is described briefly in turn.

1) Molecular Population Density Dynamics Analysis

The work completed to date in analyzing the behavior of molecular population density is far from complete. Currently, the results are based on averages or samplings, which remains to be ascertained if this causes as loss of important information. Also, a more fundamental description of the lasing threshold and saturation regions is sought.

2) System Identification Phenomenology

The reader will notice that no phenomenological equations were given with regards to the lasing profile. Although some basic fitting procedures could be applied to determine some phenomenology, the simplistic nature of those equation would not be particularly be helpful. As far as the author is aware, there have not been attempts to apply system identification methods to generate phenomenology, especially in the field of optics. By using system identification, not only will a systematically verifiable and statistically sound phenomenology be developed, but insights could be developed linking the theory presented in the introduction to the phenomenology beyond intuitive reasoning.

3) Molecular Approximation Analysis

The work presented comparing the EQF and MFA is still in inception. (The coupling of light to more than one molecule still needs to be implemented). Perhaps of most interest though are the following two things: Extension of the EQF and MFA to higher level molecules (particularly 4 levels to compare with the work in Section II-C, and to translate the algorithm developed from MATHEMATICA to FORTRAN so that hundreds or greater numbers of dipoles can be simulated, in reasonable amounts of time. Both areas will be pursued.

REFERENCES

[1]   W. A. Murray and W. L. Barnes, "Plasmonic Materials," *Advanced Materials,* vol. 19, pp. 3771-3782, 2007.

[2]   H. Ibach and H. Luth, Solid-State Physics: An Introduction to Principles of Material Science, Berlin: Springer, 2009.

[3]   A. Fang, T. Koschny and C. M. Soukoulis, "Lasing in metamaterial nanostructures," *Journal of Optics,* vol. 12, 2010.

[4]   H. A. Atwater, "The Promise of Plasmonics," *Scientific American,* vol. 296, no. 4, pp. 52-62, 2007.

[5]   M. Dridi and G. C. Schatz, "Lasing action in periodic arrays of nanoparticles," *Journal of Oticla Society of America,* vol. 32, no. 5, pp. 818-823, 2015.

[6]   M. Dridi and G. C. Schatz, "Model for describing plasmon-enhanced laser that combines rate equations with finite-difference time-domain," *Journal of Optical Society of America,* vol. 30, no. 11, pp. 2791-2797, 2013.

[7]   P. Törmä and W. L. Barnes, "Strong coupling between syrface plasmon polaritons and emitters: a review," *Reports on Progress in Physics,* vol. 78, 2015.

[8]   J. Cuerda, F. J. Garc´ıa-Vidal and J. Bravo-Abad, "Spatio-temporal modeling of lasing action in core-shell metallic nanoparticles," *ACS Photonics,* 2016.

[9]   B. J. Hunt, The Maxwellians, New York: Cornell University Press, 2005.

[10]   A. Taflove and S. C. Hagness, Computational Electrodynamcis: The Finite-Difference Time-Domain Method, Boston: Artech House, 2000.

[11]   G. R. Fowles, Introduction to Modern Optics, New York: Dover Publications, 1975.

[12]   D. J. Griffiths, Introduction to Quantum Mechanics, Upper Saddle River: Pearson, 2005.

[13]   J. D. Jackson, Classical Electrodynamics, John Wiley & Sons, 1962.

[14]   S. K. Gray and T. Kupka, "Propagation of light in metallic nanowire arrays: Finite-difference time-domain studies of silver cylinders," *Physical Review B,* vol. 68, 2003.

[15]   B. E. A. Saleh and M. C. Teich, Fundamentals of Photonics, New York: John Wiley & Sons, 1991.

[16]   A. E. Siegman, Lasers, Mill Valley: University Science Books, 1986.

APPENDIX A: FFT RESULTS

Contained in the following section – supplementary figures referred to in Section II-B2: selected spectra and various zoomed figures to observe referred to subtleties.
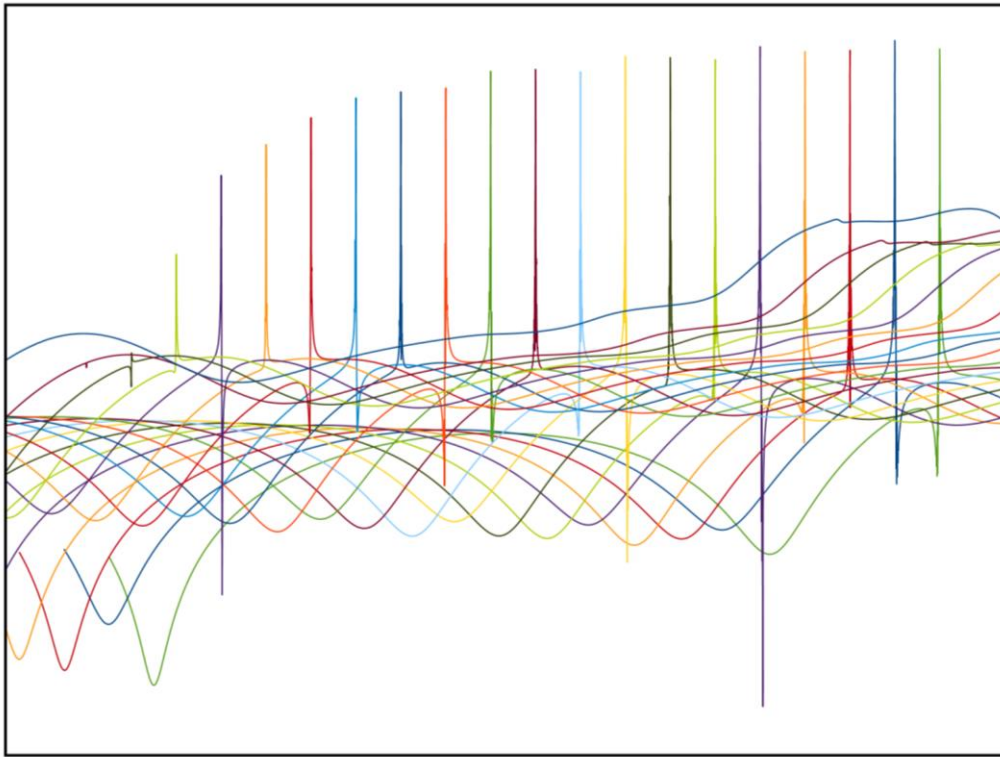
Figure 52: Detail of Figure 10 in section 2) FFT Results. E0 from $7.00d8\frac{v}{m}$ to $5.10d7\frac{v}{m}$ from left to right.
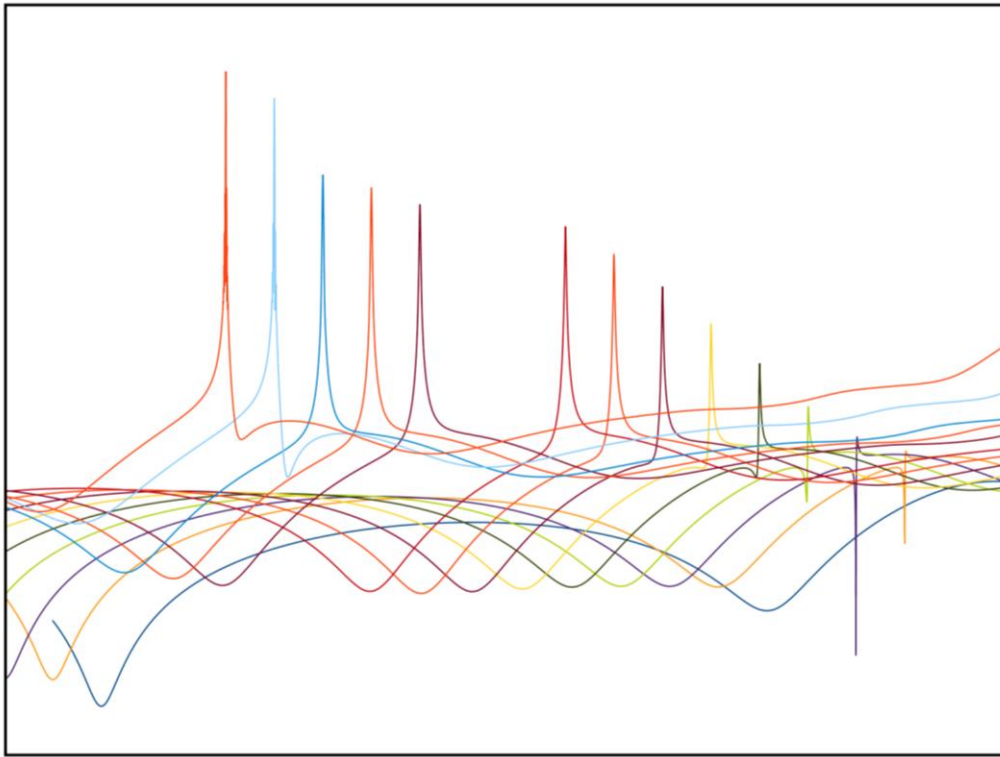
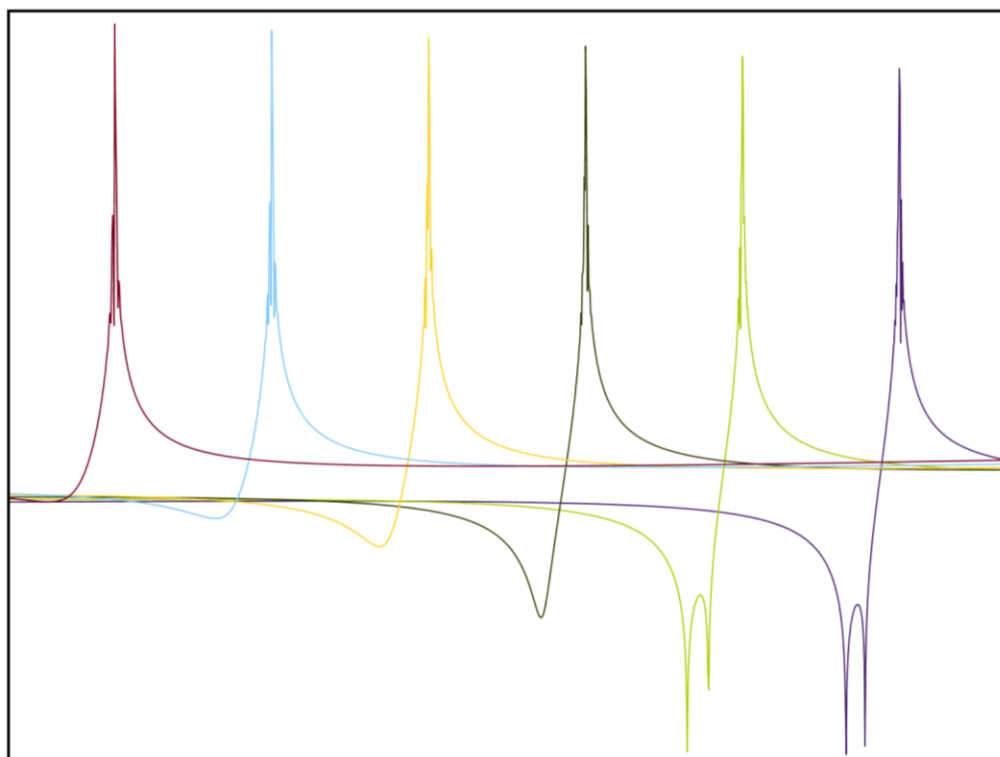Figure 53: Detail of Figure 10 in section 2) FFT Results. E0 from $9.00d7\frac{v}{m}$ to $3.00d7\frac{v}{m}$ from left to right.
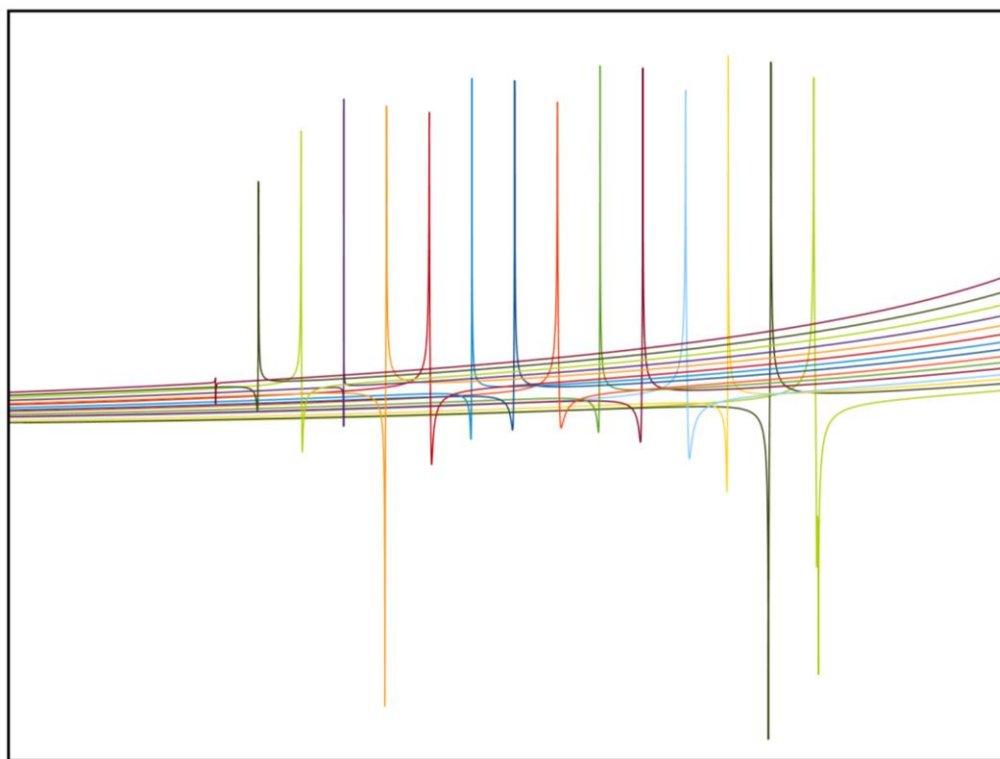
Figure 54: Detail of Figure 12 in section 2) FFT Results, E0 from $7.00d8\frac{v}{m}$ to $5.60d8\frac{v}{m}$.
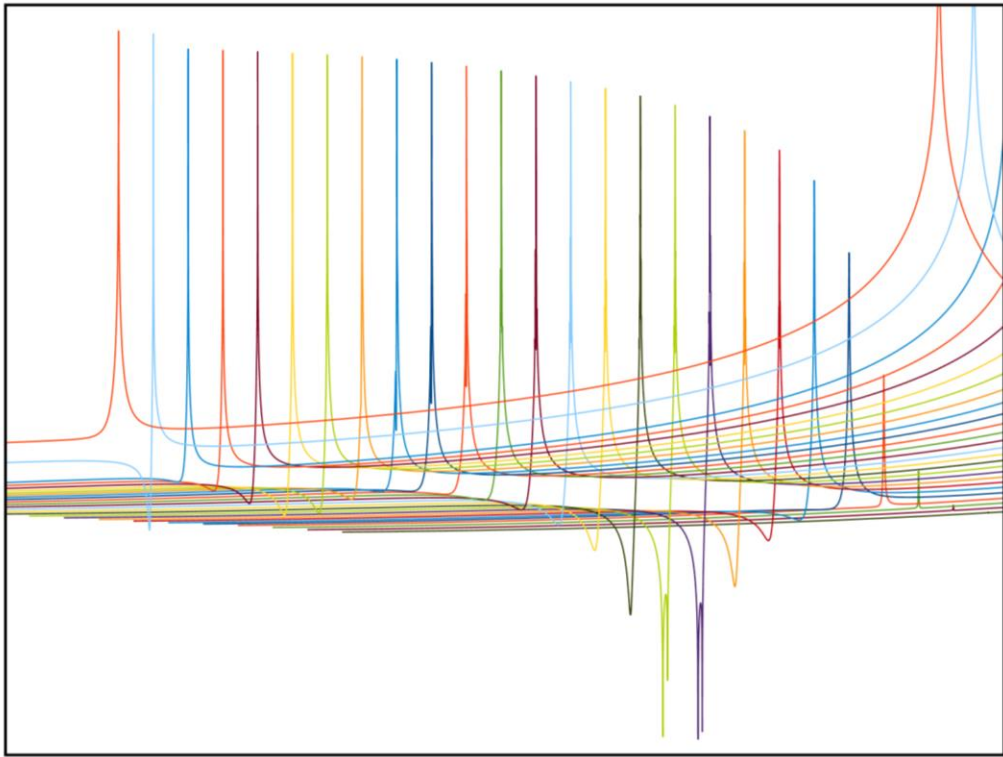
Figure 55: Detail of Figure 12 in section 2) FFT Results, E0 from $9.00d7\frac{v}{m}$ to $3.00d7\frac{v}{m}$.

Figure 56: Detail of Figure 55 highlighting some numerical graininess and remnants of transient response, E0 from $4.30d7\frac{v}{m}$ to $3.80d7\frac{v}{m}$ from left to right.
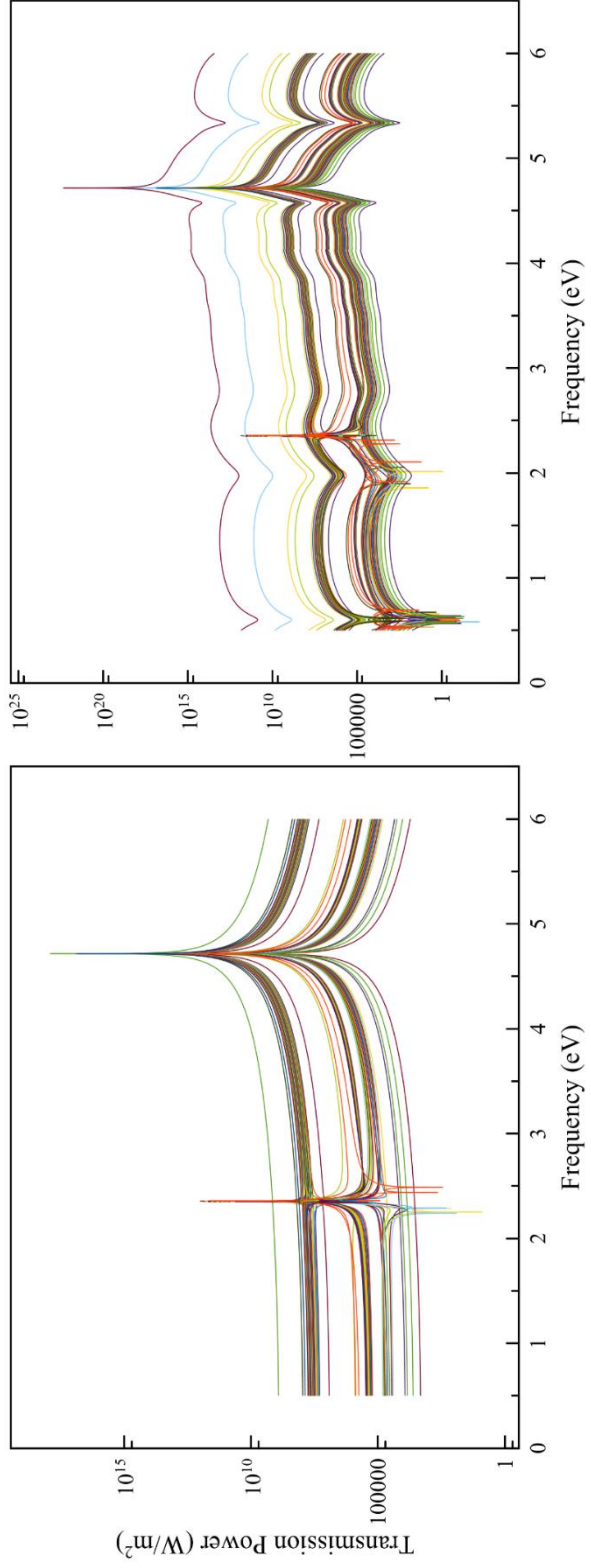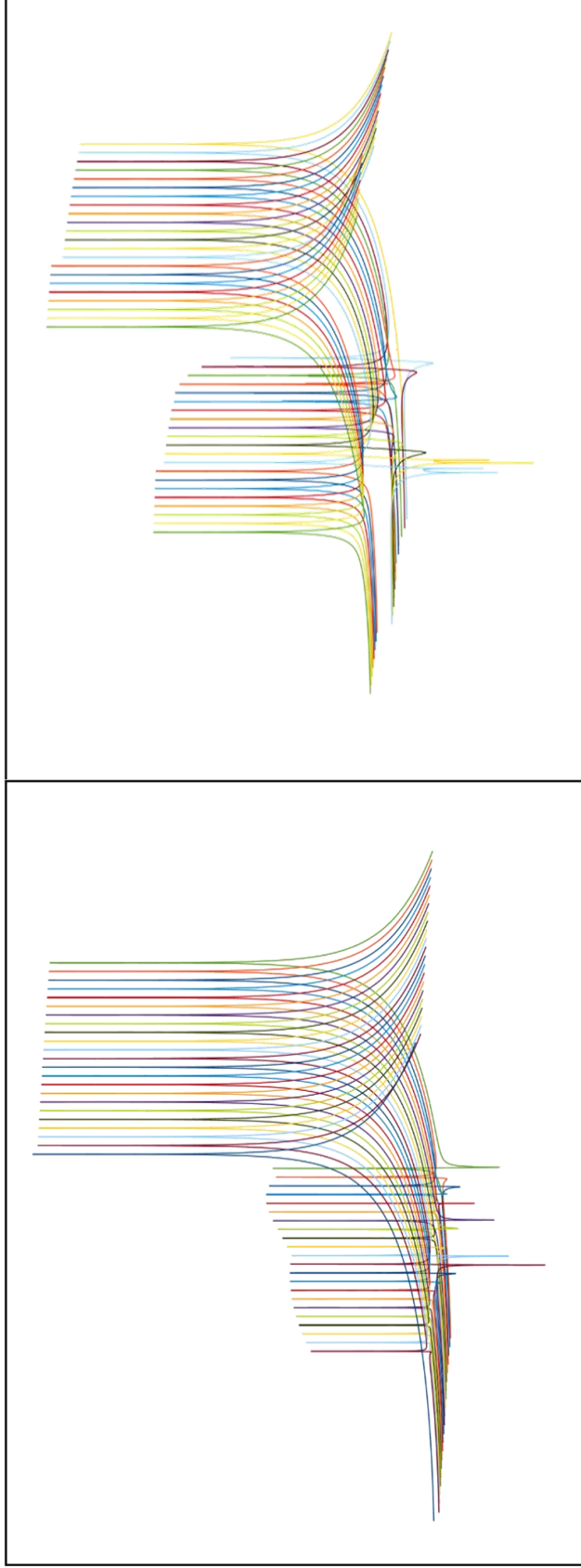
Figure 57: Complete Transient FFT spectra for Mt = 30nm. On the left (varying E0 from $5.00d6 \frac{v}{m}$ to $3.00d9 \frac{v}{m}$), the revised Spectra, on the right (varying E0 from $5.00d6 \frac{v}{m}$ to $5.00d11 \frac{v}{m}$), the transient spectra with expected transient "texture".
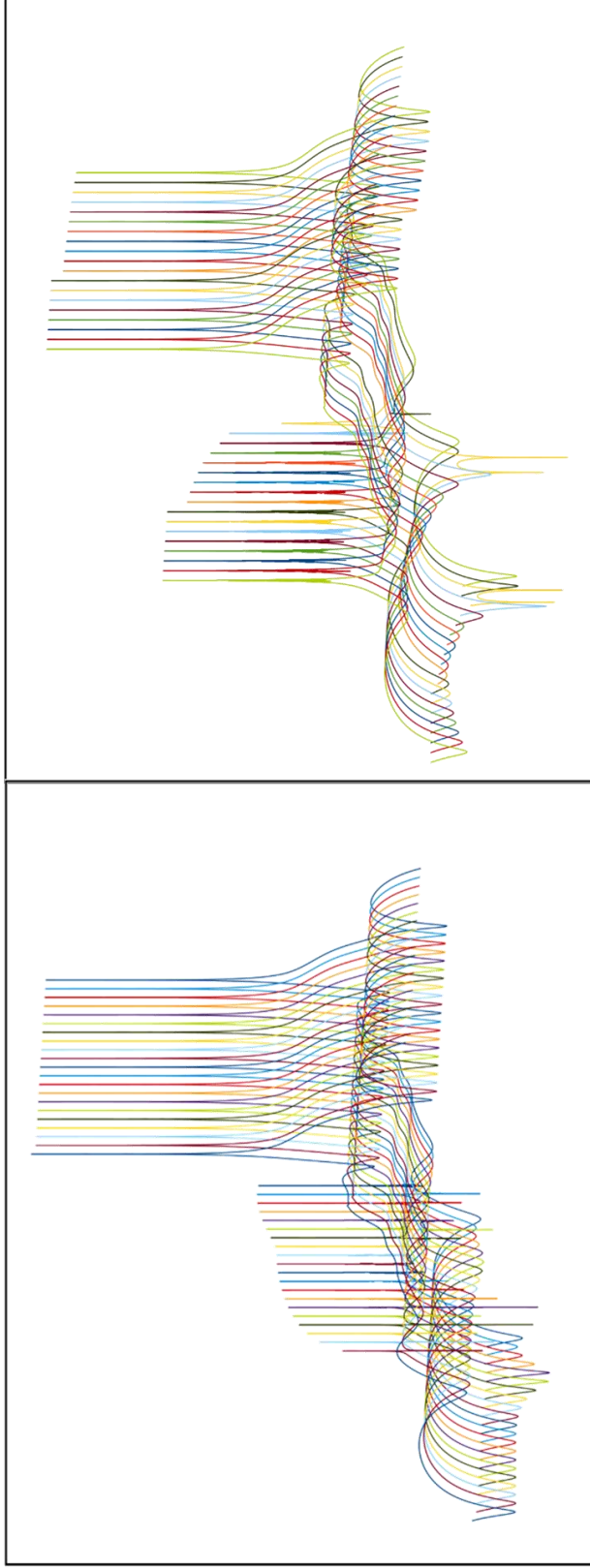
Figure 58: The left figure shows the transient Mt=30nm spectra from E0 $6.00d8\frac{v}{m}$ to $7.90d8\frac{v}{m}$ spaced out to see the decrease and disappearance of the lasing peak. The right figure shows the spectra from E0 from $2.00d7\frac{v}{m}$ to $5.00d7\frac{v}{m}$ spaced out to see the appearance and increase of the lasing peak.
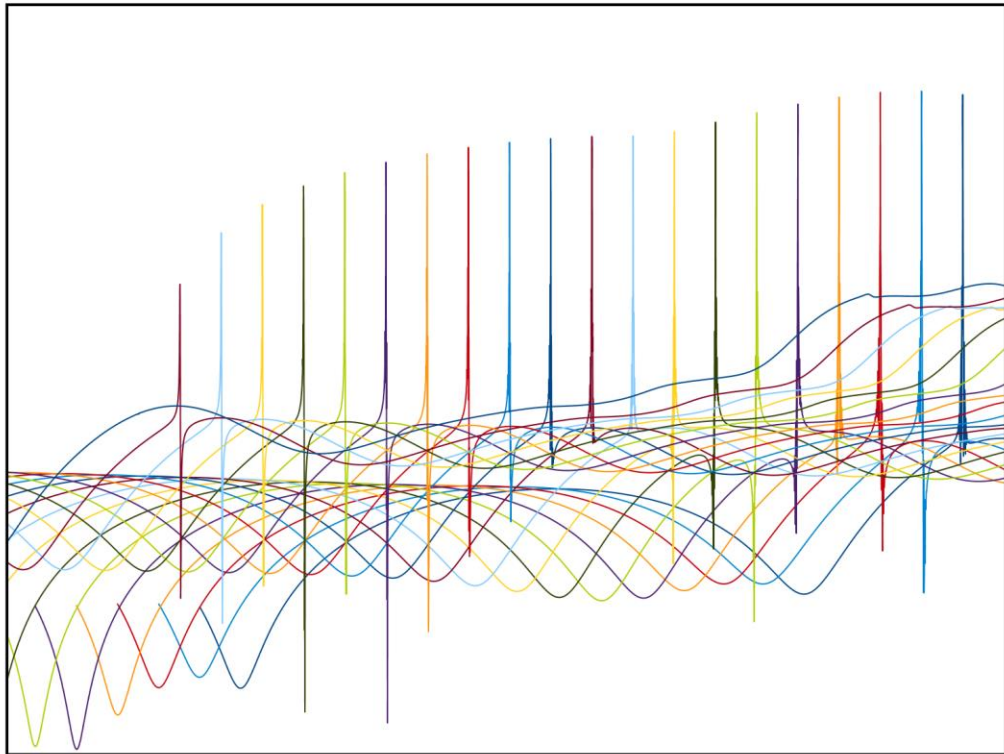
Figure 59: Detail of Figure 58, left side from $6.00d8\frac{v}{m}$ to $7.90d8\frac{v}{m}$.
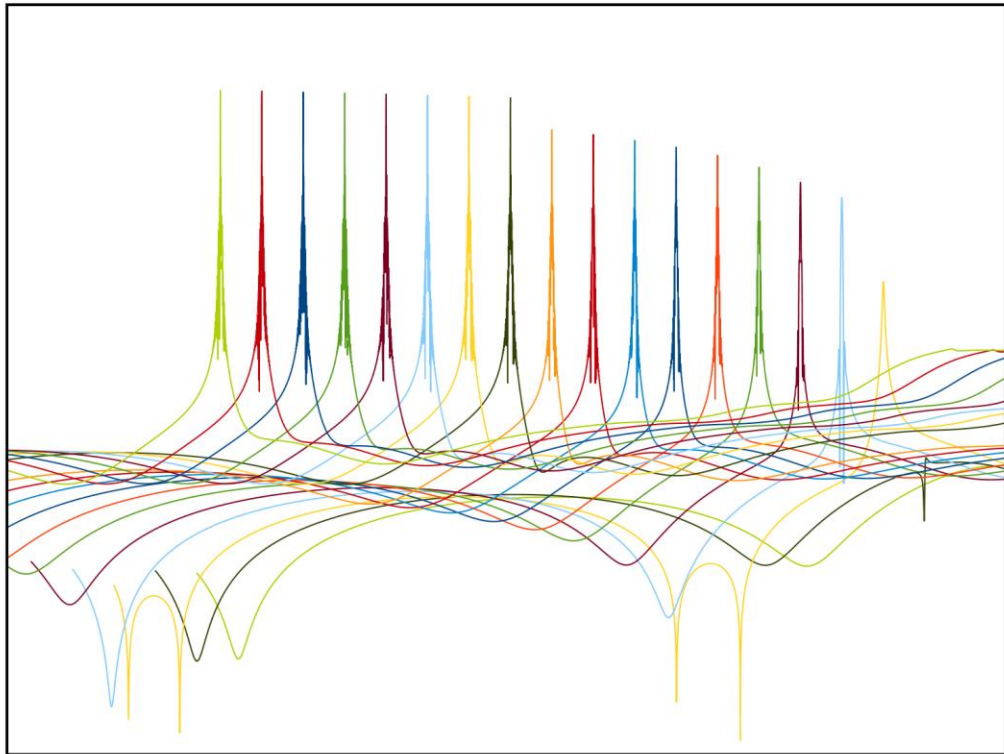
Figure 60: Detail of Figure 58, right side from $2.00d7\frac{v}{m}$ to $5.00d7\frac{v}{m}$.

Figure 61: Complete Revised FFT spectra for Mt = 30nm. On the left (varying E0 from $5.80d8\frac{v}{m}$ to $9.00d8\frac{v}{m}$), the revised Spectra, on the right (varying E0 from $1.80d7\frac{v}{m}$ to $3.00d7\frac{v}{m}$), with expected transient smoothness
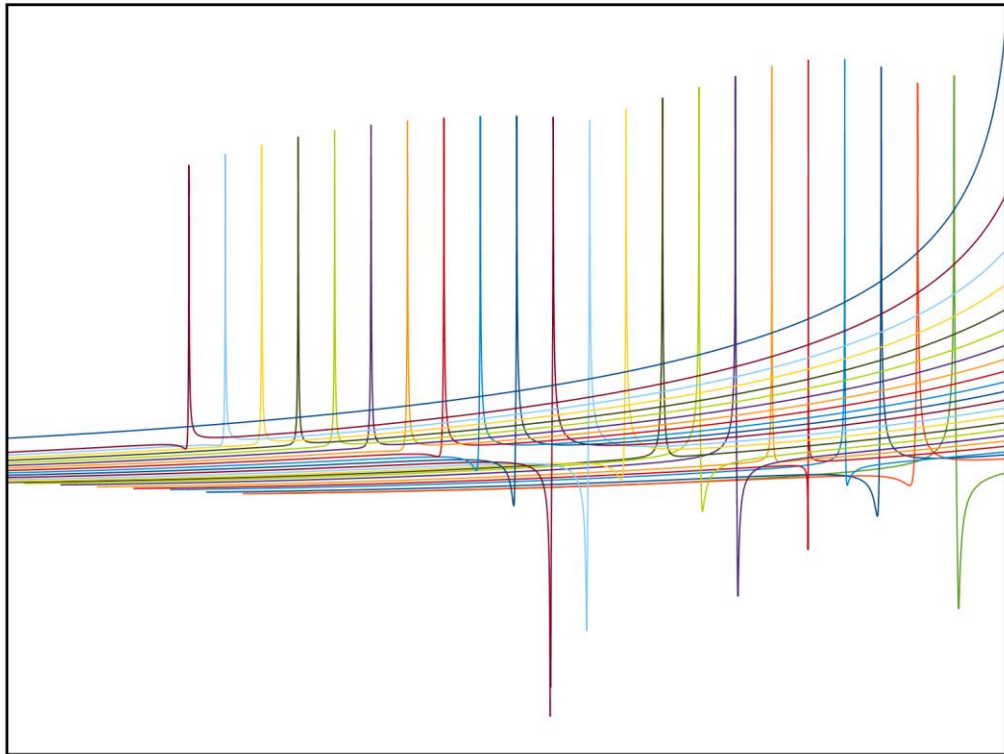
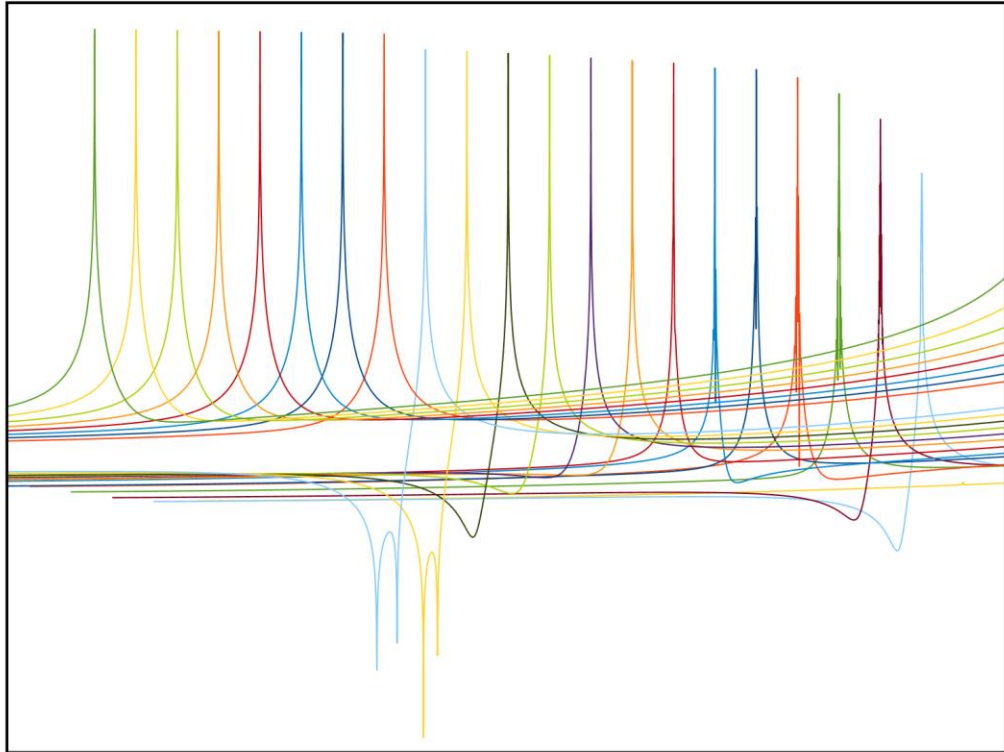Figure 62: Detail of Figure 61, left side from $5.80d8\frac{v}{m}$ to $9.00d8\frac{v}{m}$.

Figure 63: Detail of Figure 61, right side from $1.80d7\frac{v}{m}$ to $3.00d7\frac{v}{m}$.

APPENDIX B: LASING PROFILES

Contained in the following section – supplementary figures referred to in Section II-B3.
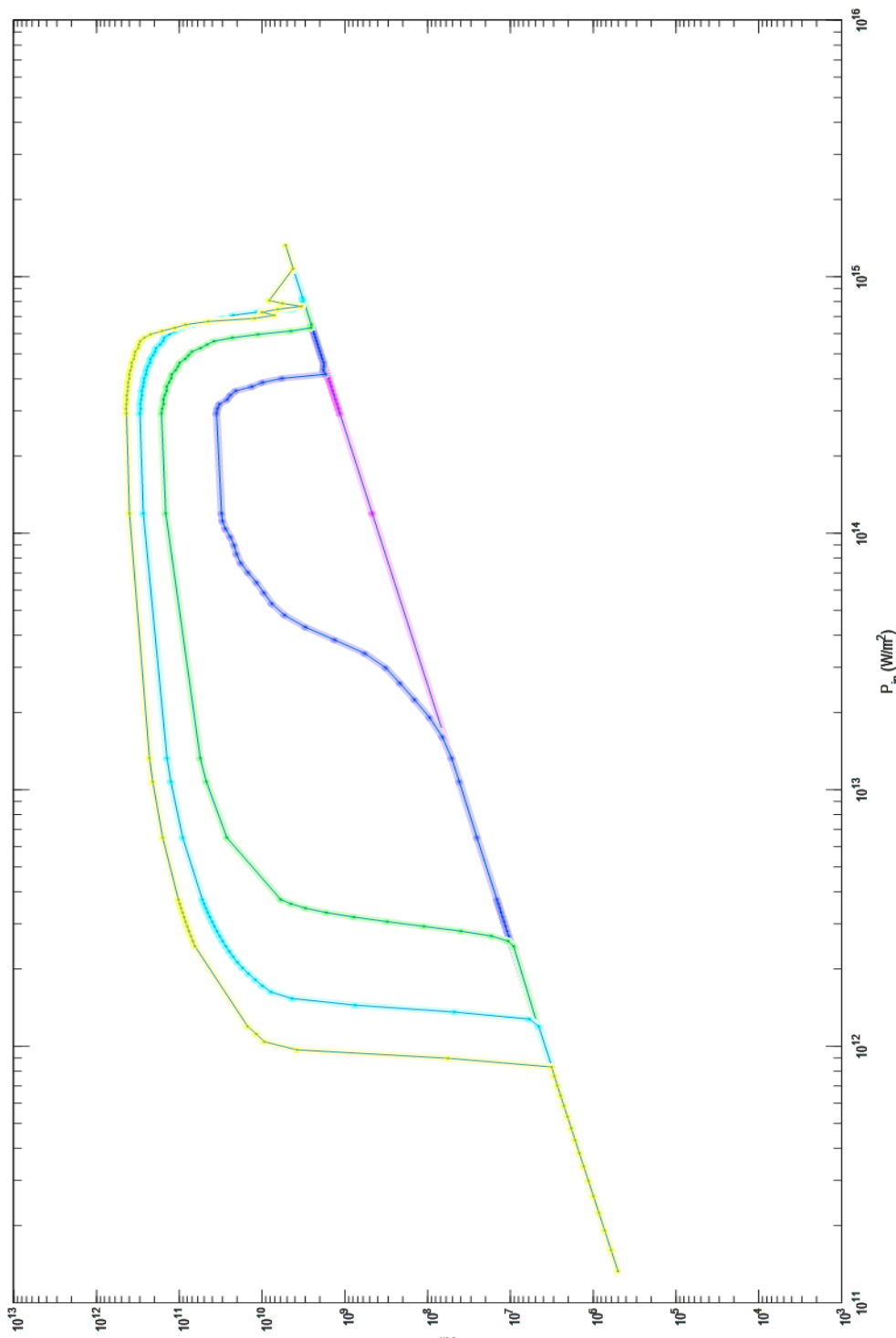
Figure 64: Lasing Profiles varying in nD. Purple: 3.0d24 | Blue: 3.5d24 | Green: 4.0d24 | Cyan: 4.5d24 | Yellow: 5.0d24
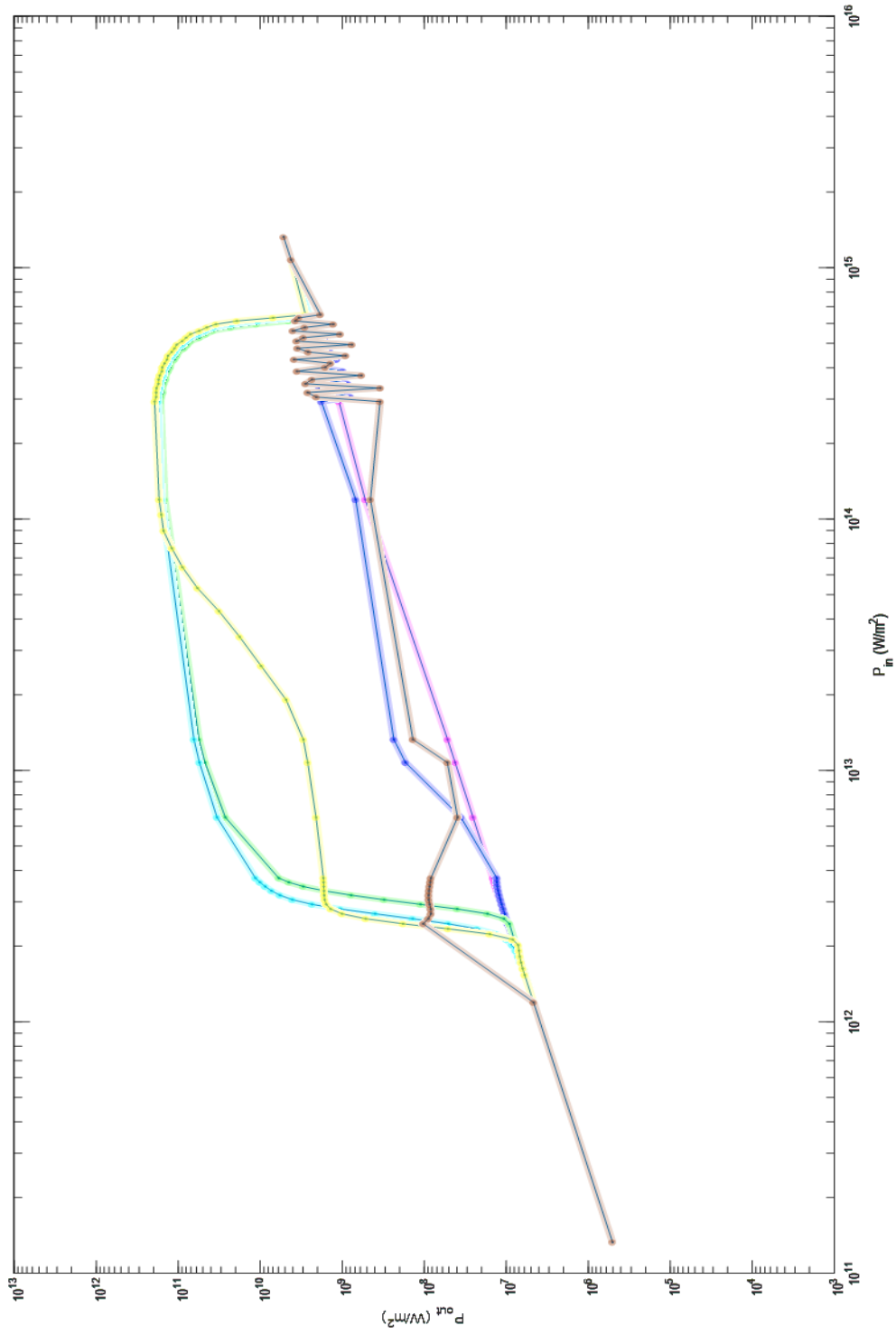
Figure 65: Lasing Profiles varying in $\omega_{2\leftrightarrow1}$. Purple: 2.300 eV | Blue: 2.340 eV | Green: 2.358 eV | Cyan: 2.365 eV | Yellow: 2.372 eV | Brown: 2.380 eV